Applied Thermal Engineering 304 (2026) 132615

Contents lists available at ScienceDirect

Applied Thermal Engineering

journal homepage: www.elsevier.com/locate/ate

Research Paper

Effect of strut inclination on thermo-hydraulic performance of X-type lattice heat sinks: A numerical study

Ebelechukwu Okeke, Mehdi Khatamifar *, Wenxian Lin

College of Science & Engineering, James Cook University, Townsville, QLD 4811, Australia

ARTICLE INFO

Keywords:
X-type lattice structures
Heat transfer
Periodic cellular structure
Pressure-drop
Thermo-hydraulic performance

ABSTRACT

A numerical study was conducted to examine the influence of strut curvature angle α (40°–60°) and inclination angle β (30°–40°), on flow structure, convective heat transfer, pressure drop, pumping power, and overall thermo-hydraulic performance of X-type lattice structure over a wide Reynolds number range (Re ≈ 2645–7936). For all configurations, the average Nusselt number (Nu_{avg}) was found to increase monotonically with Re, while the pressure drop and pumping power per unit length rises more rapidly, resulting in a gradual reduction in thermal-hydraulic performance at higher Re. α was identified as the dominant geometric factor: decreasing α enhances convective heat transfer through stronger geometric confinement, intensified flow acceleration and deflection, and larger thermal gradients within the lattice core, although it also increases pressure losses and pumping power. In contrast, the influence of β is relatively minor and primarily serves to fine-tune the flow and thermal fields. Overall, improved performance can be achieved at small α and moderate Re, where convective heat transfer enhancement outweighs hydraulic losses, indicating that balanced geometric design, rather than maximization of individual lattice angles or heat transfer metrics, is essential for achieving high-performance lattice heat sinks. Excellent correlations were developed for Nu_{avg}, pressure drop per unit length, pumping power per unit length and thermal-hydraulic performance factor to quantify the combined effects of Re, α and β. These findings provide insight into the thermo-hydraulic behaviour of additively manufactured lattice-based thermal-management systems for compact and energy-efficient engineering applications.

1. Introduction

The relentless increase in heat generated by modern electronics, aerospace, and energy-conversion systems has outpaced the capabilities of traditional thermal-management solutions, such as pin fins, plate fins, and stochastic metal foams. These conventional means often face a trade off between achieving high heat transfer rates and maintaining acceptable pressure drops under stringent size, weight, and pumping power constraints [1,2]. Periodic cellular structures have emerged as a promising class of multifunctional structures that combine high specific surface area, tailored flow paths, and load-bearing capability, making them ideal for next-generation compact heat exchangers, and heat transfer capabilities [3]. Among periodic lattice geometries, the cubic lattice [4,5], face-centred cubic (FCC), body-centred cubic (BCC), octet truss [6–8], Pyramidal lattice [9–11] and tetrakaidecahedron (TKD) topologies have been widely studied for their convective and conductive heat transfer characteristics [12,13]. Representative periodic lattice structures commonly investigated for thermal-management applications are illustrated in Fig. 1

Experimental and numerical investigations have demonstrated that, at comparable porosities, these uniform lattices can achieve the Nusselt numbers (Nu) up to an order of magnitude higher than smooth channels, owing to enhanced mixing, disruption of thermal boundary layers, and substantial internal surface area [14,15]. Recent studies have further probed how specific geometric parameters (ligament width, pore density, and unit-cell length) control the Nu-Re relationship and pressure-drop (where Re is the Reynolds number). Ho et al. [16] examined forced convection in Rhombi-Octet lattice blocks manufactured via selective laser melting, finding that decreasing ligament width (increasing pore density) raises both Nu and pressure drop; nonetheless, lattice blocks achieved Colburn j-factors and thermal efficiency indices exceeding those of commercial metallic foams and conventional pin-fins. Similarly, Aider et al. [14] compared Octet, Face diagonal cube (FD-Cube), TKD, and simple cubic lattices at porosity of ~0.88, observing that thermally developing flow requires ~5–6 unit-cell lengths and that, when using pore-scale reference lengths, Nu-Re data for diverse

* Corresponding author.
E-mail address: mehdi.khatamifar2@jcu.edu.au (M. Khatamifar).

https://doi.org/10.1016/j.applthermaleng.2026.132615
Received 7 April 2026; Received in revised form 27 July 2026; Accepted 29 July 2026
Available online 6 August 2026
1359-4311/© 2026 The Authors. Published by Elsevier Ltd. This is an open access article under the CC BY license (http://creativecommons.org/licenses/by/4.0/).

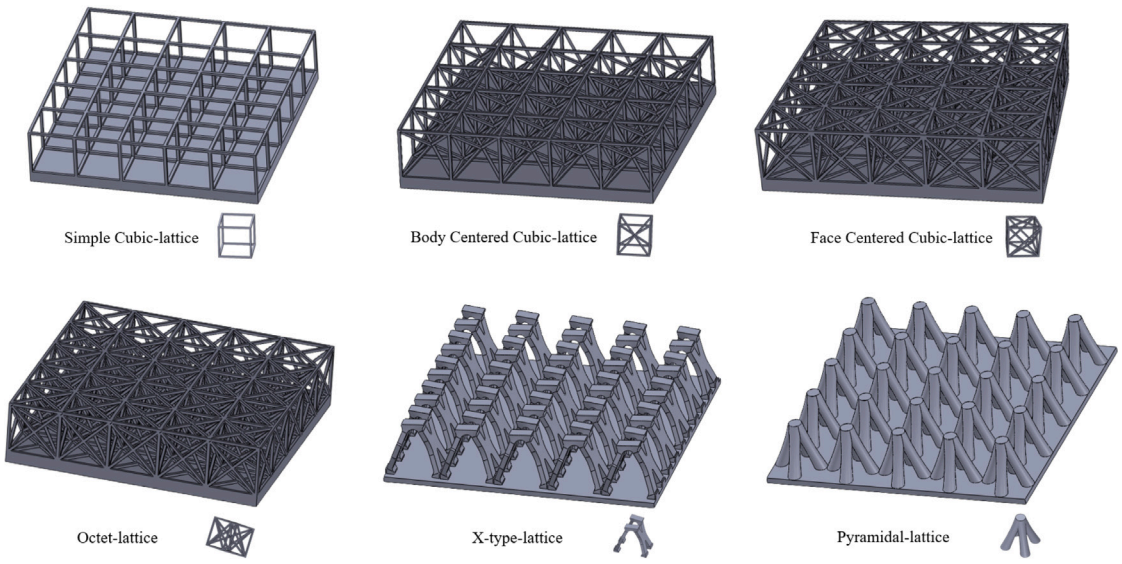


Fig. 1. Periodic lattice structures for thermal-management and lightweight structural applications.

topologies collapse to a single correlation, facilitating unified performance predictions. Likewise, Shahrzadi et al. [2] studied heat transfer in BCC lattices across conduction, convection, and radiation modes via detailed numerical simulations, revealing that radiative effects become dominant at high porosities (>0.90) and elevated temperatures, and quantifying the interplay between Re, porosity, and effective thermal conductivity.

X-type metallic lattices represent a particularly attractive variant of periodic cellular materials. Early studies on sandwich panels cored with X-lattices highlighted their superior heat dissipation performance compared to competing topologies such as pyramidal, tetrahedral, and Kagome cores. Jin et al. [17] conducted a detailed numerical study to compare X-lattice and pyramidal-lattice sandwich panels at matched porosity and surface-area density, reporting a 47%–60% higher overall Nu and 75%–97% enhancement in endwall heat transfer for the X-lattice configuration over Re_H = 3100–5700, where Re_H is the Reynolds number with height as the characteristic length. They attributed this improvement to the counter-rotating spiral primary flows and complex secondary vortices induced by the staggered ligaments intersections, which intensify convective exchange on both ligaments and facesheets. Complementary experimental work by Yan et al. [18] validated these numerical trends in a lightweight X-lattice cored sandwich panel, demonstrating up to 38% higher Nu than tetrahedral lattices and comparable performance to Kagome cores, while also exhibiting significantly lower pressure drop for a given pumping power. They further clarified that, despite limited flow mixing relative to ligament-based lattices, the greater surface-area density inherent to the X-type arrangement is the primary enabler of its enhanced thermal performance.

Preliminary insights from biomechanics and structural-mechanics literature suggest that angle tuning can strongly affect permeability, effective thermal conductivity, and mechanical stiffness in beam-based lattices [19]. The intersection angle is known to critically influence flow path tortuosity, ligament surface inclination, and the formation of primary and secondary vortices; all of which govern convective heat transfer and frictional losses. Despite the considerable research on periodic lattices, most studies to date have focused on fixed ligament orientations (static α and β angles, where α is the strut curvature angle and β is the strut inclination angle, as shown in Fig. 2) and unit-cell shapes. For instance, Jin et al. [17] and Yan et al. [18], in their works on X-type lattices, considered only the α of 50° and β of 42° between ligaments. Understanding the thermo-hydraulic consequences of varying the X-lattice angles for forced convection applications, particularly under conditions of constant pumping power and within the transitional/turbulent Re regimes relevant to applications, including electronic cooling, is essential for unlocking the full design space of X-type cores.

In this work, a comprehensive numerical investigation of X-type lattice heat sinks with systematically varied crossing angles was carried out using validated models with ANSYS Fluent, to obtain pressure drop, local and average Nu, and flow fields for α ranging from 40° to 60° at matched porosities and ligament dimensions. The objectives of the present study are to elucidate how angle variation alters primary flow spirals, vortex structures, and local heat transfer distributions, quantify the trade-off between enhanced surface-area projections and increased friction factor, and identify optimal angle configurations for maximum thermo-hydraulic performance under fixed pumping power constraints. It should be noted that, in addition to the strut-curvature angle (α) and strut-inclination angle (β), other geometric parameters such as ligament thickness, unit-cell dimensions, and porosity can also significantly influence the thermo-hydraulic behaviour of X-type lattice structures. In the present study, these parameters were intentionally maintained constant in order to isolate the effects of α and β on the flow structure, heat transfer, and pressure-drop behaviour. Simultaneous variation of multiple geometric parameters would introduce additional coupled effects associated with changes in surface-area density, flow blockage, and hydraulic diameter, thereby making it difficult to distinguish whether the observed thermo-hydraulic changes originated from variations in α and β or from concurrent changes in other geometric characteristics. The adopted approach therefore provides a controlled parametric framework for systematically evaluating the thermo-hydraulic effects of angle variation within X-type lattice heat sinks. Nevertheless, future investigations involving coupled optimization of additional geometric parameters remain an important direction for further investigation. By leveraging insights from prior fixed-angle X-lattice studies [17,18], as well as broader lattice literature on angle-dependent transport in porous media [20] and unified correlations for diverse topologies [14], this study aims to provide practical design guidelines and a deeper physical understanding of the angle effects in X-type heat sinks. The results will facilitate targeted tailoring of lattice cores to specific application requirements, enabling compact, lightweight, and highly efficient thermal management solutions for the next generation of high-power, high-density systems.

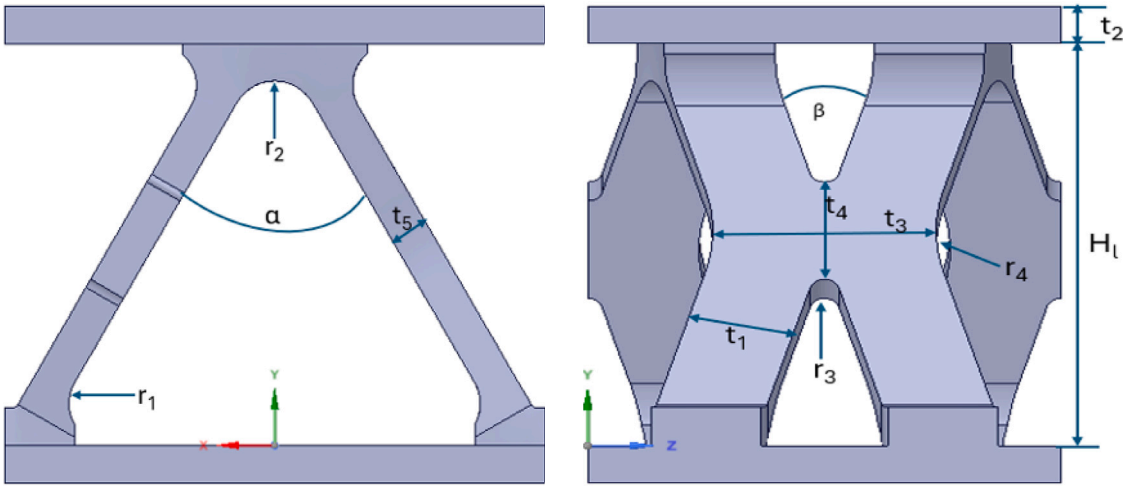


Fig. 2. X-type lattice: (a) Front view and (b) Side view.

2. Methodology

2.1. X-type lattice unit cell model

The X-type lattice unit cell considered in the present study was modelled in SolidWorks with the strut curvature angle (α) and the strut inclination angle (β) varied. α is the angle formed by the outer curved surfaces of the two struts in the lattice, as shown in the front view in Fig. 2(a), and β is the angle formed by the inner, intersecting surfaces of the two struts, visible in the side view in Fig. 2(b). A fillet of 1 mm radius was created between the core and the substrate, as that in [18], to remove the curved surface between two. Five α values (40°, 45°, 50°, 55°, and 60°) are considered and for each α value, three β values are considered (30°, 36° and 40°). The remaining geometric parameters were held constant for all models: r_1 = 1.00 mm, r_2 = 1.05 mm, r_3 = 2.70 mm, r_4 = 4.30 mm, t_1 = 2.16 mm, t_2 = 0.90 mm, t_3 = 2.70 mm, t_4 = 2.31 mm, and t_5 = 0.91 mm, respectively. The generated geometry was imported into ANSYS SpaceClaim for repair and preparation. Here, short channels having the same height as the geometry and a length of 10 mm were created at the inlet and outlet of the domain.

2.2. Governing equation, computational domain and boundary conditions

The governing equations for the steady, three-dimensional, incompressible flow and heat-transfer processes used in the present study are as follows [17,21].

Continuity equation:

$$\frac{\partial u_i}{\partial x_i} = 0 \tag{1}$$

Momentum equation:

$$\rho_f u_j \frac{\partial u_i}{\partial x_j} = -\frac{\partial p}{\partial x_i} + \frac{\partial}{\partial x_j}\left[(\mu + \mu_t)\left(\frac{\partial u_i}{\partial x_j} + \frac{\partial u_j}{\partial x_i}\right)\right] \tag{2}$$

Energy equations for the fluid and solid domains:

$$\frac{\partial(\rho_f c_{p,f} u_j T_f)}{\partial x_j} = \frac{\partial}{\partial x_j}\left[(k_f + k_t)\frac{\partial T_f}{\partial x_j}\right] \quad \text{(fluid domain)} \tag{3}$$

$$\frac{\partial}{\partial x_j}\left(k_s \frac{\partial T_s}{\partial x_j}\right) = 0 \quad \text{(solid domain)} \tag{4}$$

where x_i and x_j are the Cartesian coordinate components, and u_i and u_j are the velocity components in the corresponding directions, p is the pressure, T_f and T_s are the fluid and solid temperatures, ρ_f and $c_{p,f}$ are the specific heat capacity of the fluid, k_f and k_s are the thermal conductivities of the fluid and solid domains, μ is the dynamic viscosity, and μ_t and k_t are the turbulent viscosity and turbulent thermal conductivity, respectively. The standard shear stress transport (SST) $k-\omega$ turbulence model was used to simulate the turbulence effects. As the equations for the SST $k-\omega$ turbulence model has been well documented (e.g. [17]), they are not presented here to avoid repetition.

A single periodic slice of five cells in the streamwise direction and one cell in the transverse direction is modelled, exploiting symmetry to halve the domain. The computational domain, flow direction, periodic boundaries, symmetry plane, and thermal boundary conditions of the empty channel and the primary X-type lattice model are illustrated in Figs. 3 and 4.

Meshing was generated in ANSYS (2023 R2). For the inlet boundary condition, a fully developed velocity profile with a uniform temperature T_{in} was applied. To obtain the fully developed velocity profile, an empty channel was firstly simulated. The inlet and outlet of the channel were set to be translational periodic specifying mass flow rate. Symmetry boundary condition was enforced on the two sides of the channel, while the other sides were set as adiabatic, as shown in Fig. 3. For the outlet of the primary domain, a pressure-outlet specifying zero guage pressure was applied. A translational periodic boundary condition specifying zero-pressure gradient was enforced at the two side surfaces to mimic an infinite lattice array. Uniform heat-flux (q'') was applied on the bottom substrate and other walls were set as no-slip adiabatic walls. Conjugate-heat-transfer coupling applies.

All simulations assume steady, three-dimensional, and incompressible flow of air with constant properties at T_{in}, and neglect buoyancy and viscous dissipation. The simulations were carried out using Ansys Fluent (2023 R2), with air as the working fluid. The thermal and physical properties of the fluid and solid were kept constant according to [22,23]. A constant heat flux of 6000 W/m^2 was applied to the bottom surface of the plate. Prior to selecting the appropriate numerical simulation model, it is essential to determine the prevailing flow regime. Within the velocity range considered in this study, the Reynolds number, defined based on the channel height, ranges from 2645 to 7935. Although different Reynolds number definitions are used in the literature for porous and lattice structures, these values correspond to a regime where inertial effects are dominant and strong flow mixing occurs within the lattice core [24]. Such behaviour is characteristic of turbulent flow in complex geometries. Therefore, the flow in the present study is treated as turbulent, and turbulence is

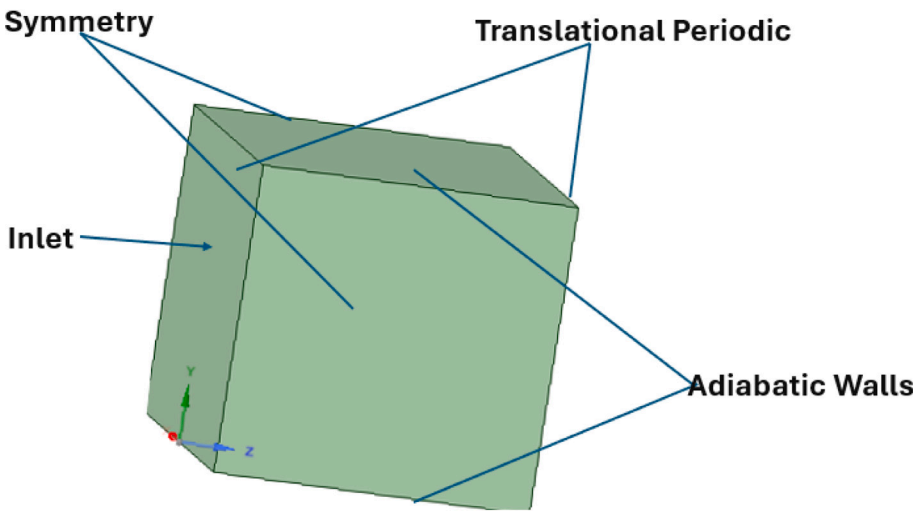


Fig. 3. Boundary conditions of the empty channel.

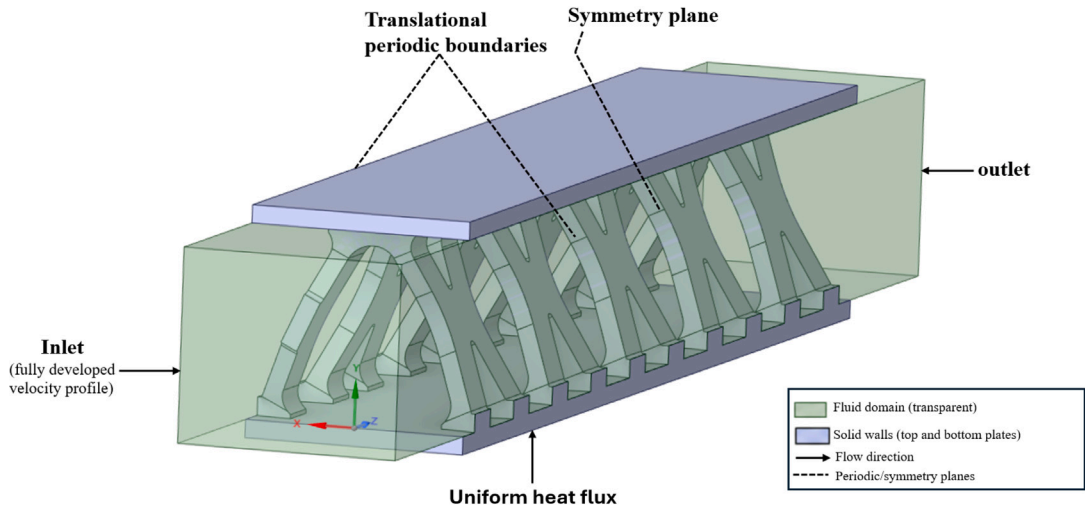


Fig. 4. Computational domain and boundary conditions for the five-unit-cell X-type lattice configuration used in the numerical simulations.

modelled using the SST k–ω, same as some of the previous lattice CFD studies (e.g., [18,24]), which is well suited for resolving near-wall regions and capturing flow separation in complex geometries.

2.3. Mesh generation and independency test

High quality mesh was generated for the lattice structure model to balance computational cost with solution accuracy. To achieve this, the body sizing of 0.0005 m, 14 layers of inflation with the transition ratio of 0.1, and the growth rate of 1.05, were set at the fluid–solid interface to capture the near wall velocity. Edge sizing was used for the edges of the geometry specifying number of divisions. A mesh produced is shown in Fig. 5 as an example.

A mesh-independence study was conducted at the highest Re (Re = 7936) considered in the present work, where the flow and thermal gradients are most demanding. Six computational meshes containing 3,140,000, 7,078,811, 10,814,543, 12,529,893, 14,305,964, and 17,266,977 elements were generated. The corresponding Nu_{avg} was calculated using Eq. (9), with the local Nusselt numbers (Nu_{loc}) evaluated at five axial positions along the flow direction using Eq. (6), corresponding to z/L = 0.1, 0.3, 0.5, 0.7, and 0.9, as defined below. The pressure drop (ΔP) was calculated as the difference between the area-weighted static pressures at the inlet and outlet surfaces for each mesh. The resulting mesh-independency data are presented in Table 1. As shown, the predicted pressure drop increases with mesh refinement, while the Nusselt number decreases. This opposite trend is expected, as coarse meshes tend to underpredict flow resistance while overestimating thermal gradients near the wall. With further mesh refinement, both quantities converge to nearly constant values. As shown in Table 1 the variations in both Nu_{avg} and ΔP between the mesh with 14,305,964 elements and finer meshes are negligible (less than 0.5%), indicating mesh-independence behaviour. Therefore, the mesh with 14,305,964 elements was selected for all subsequent simulations, as it provides a suitable balance between computational cost and numerical accuracy. For all simulations the y^+ values are below 1.

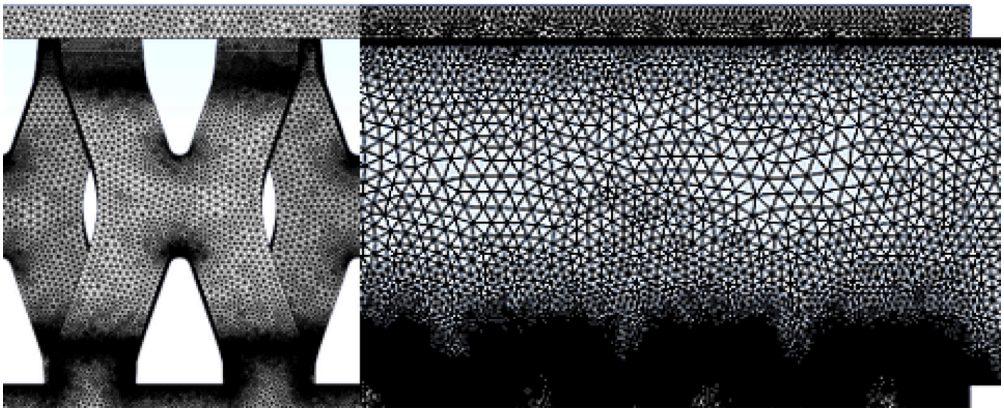


Fig. 5. Mesh generated for the X-type lattice.

Table 1
Mesh-independence study at the highest Re = 7936.

Number of elements	Nu_{avg}	ΔP (Pa)
3,140,000	263.1638	120.0000
7,078,811	249.4219	128.3960
10,814,543	235.0299	135.0302
12,529,893	222.8001	134.8523
14,305,964	222.7134	134.7822
17,266,977	222.6878	134.2649

2.4. Solution strategy

The governing equations were solved using the pressure-based solver with the coupled algorithm for pressure–velocity coupling. Second-order discretization schemes were applied for momentum, energy, and turbulence equations to ensure solution accuracy. The details are not presented here as they are standard in Ansys Fluent (2023 R2). Convergence criteria were set for all residuals to be below 1×10^{-6}.

The Reynolds number is defined using the channel height (H = 0.00966 m) as the characteristic length, i.e;

$$Re = \frac{\rho u_{in} H}{\mu} \tag{5}$$

where ρ and μ are the density and dynamic viscosity of air, and u_{in} is the prescribed inlet velocity imposed through the fully developed inlet-flow profile, respectively. This definition provides a consistent superficial Reynolds number across all configurations because the channel height is fixed, while the inlet velocity is prescribed and identical across cases. Variations in α modify the channel width and lattice confinement; however, using a constant H-based Re enables direct comparison of thermal-hydraulic trends under the same imposed inlet velocity and height-based length scale [18].

The local heat transfer (local Nusselt number Nu_{loc}) at z along the flow direction is defined as follows [18],

$$Nu_{loc}(z) = \frac{h(0,0,z)\, H}{k_f} \tag{6}$$

where k_f is the thermal conductivity of air and $h(0,0,z)$ is calculated by

$$h(0,0,z) = \frac{q''}{T_w(0,0,z) - T_b(z)} \tag{7}$$

in which q'' is the applied heat flux, $T_w(0,0,z)$ is the inner surface temperature of the facesheet extracted from the isosurfaces in Ansys Fluent, and $T_b(z)$ is the local bulk mean fluid temperature which was obtained from an energy balance assuming uniform heat flux,

$$T_b(z) = T_{in} + \frac{z\, q''}{q\, U_{in}\, H\, c_p} \tag{8}$$

where T_{in} is the inlet temperature, U_{in} is the inlet velocity, c_p is the specific heat of air, and z is the coordinate in the flow direction.

In addition, the averaged Nusselt number (Nu_{avg}) is obtained as the arithmetic mean of five local Nusselt numbers evaluated along the streamwise direction [18],

$$Nu_{avg} = \frac{1}{5} \sum_{i=1}^{5} Nu_{loc}(z_i), \tag{9}$$

where the local Nusselt numbers are evaluated at five axial positions along the flow direction, corresponding to z/L = 0.1, 0.3, 0.5, 0.7, and 0.9, where L denotes the length of the computational domain in the flow direction.

2.5. Model validation

To ensure the accuracy and reliability of the computational approach, the present numerical model was validated against the study of Yan et al. [24], which serves as the reference case. This reference case was selected because it employs a geometrically similar X-type lattice configuration, comparable thermal boundary conditions, and a similar Reynolds-number range to the present study. The validation was performed in two stages, focusing on both hydrodynamic and thermal aspects of flow within the X-type lattice structure. First, the inlet velocity profile was reproduced by simulating an empty channel and mapping the fully developed flow field onto the inlet of the lattice domain. As shown in Fig. 6, the predicted velocity profiles at two representative bulk velocities (Um = 4.15 m/s and Um = 11.60 m/s) exhibit good agreement with the reported data in the study [24]. The agreement is particularly strong in the core flow region, while slightly larger deviations are observed near the wall regions. These discrepancies are expected and may arise from differences in geometry reconstruction, near-wall treatment, turbulence-model implementation, and numerical discretization, as Yan et al. [24] did not present such details in their paper. In lattice structures, small variations in local geometry and inlet-flow development can significantly influence the near-wall velocity gradients and secondary-flow structures. Nevertheless, the present model successfully captures the overall shape and development of the velocity profiles, including the centreline outlet velocity (U_{co}), which is used as a reference quantity in Yan et al. [24], with less than 0.4% deviation and boundary layer behaviour, confirming its capability to reproduce the inlet flow characteristics required for reliable heat transfer predictions.

To further validate the thermal performance, the average Nusselt number (Nu_H) was compared with the numerical results reported by Yan et al. [24]. over a range of Reynolds numbers. The comparison is presented in Fig. 7. The present predictions are in good agreement with the reference data, with deviations ranging from approximately 0.5% to 5.5% across the investigated Reynolds number range. Specifically,

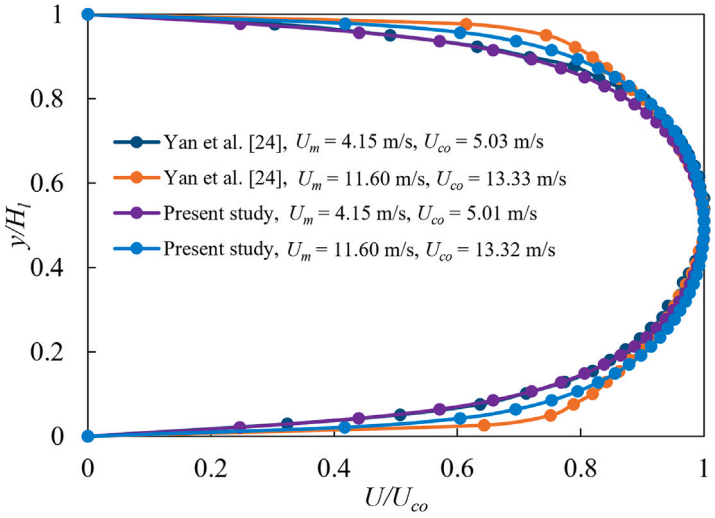


Fig. 6. Comparison of the numerical results of the inlet velocity profile between that obtained by the present study and that by Yan et al. [24].

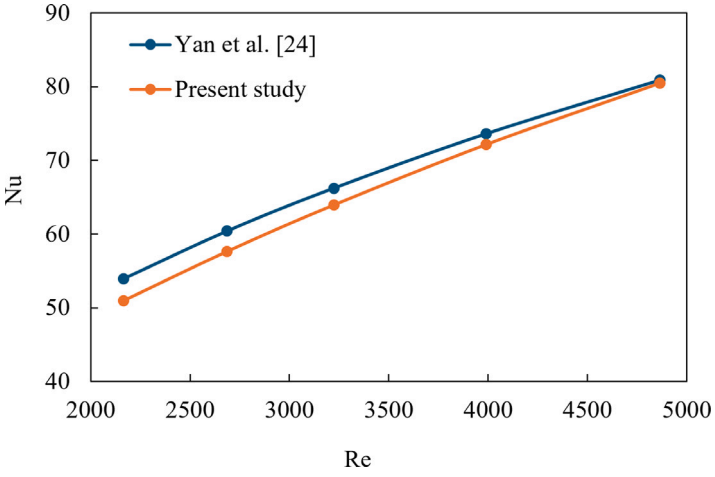


Fig. 7. Comparison of the numerical results of the Nusselt number between that obtained by the present study and that by Yan et al. [24].

the predicted Nusselt numbers are slightly lower than the reported values, particularly at lower Reynolds numbers, while the discrepancy decreases as the Reynolds number increases. Because thermo-fluid transport within lattice structures is strongly influenced by confined flow acceleration, boundary-layer interaction, vortex formation, and local secondary-flow development [24,25], small discrepancies between different computational studies are commonly observed even under nominally similar operating conditions. Importantly, the present model accurately reproduces the monotonic increase of the Nusselt number with Reynolds number, as well as the overall trend and curvature of the reference data. Overall, the good agreement obtained for both hydrodynamic and thermal quantities provides confidence in the accuracy and reliability of the present numerical methodology for predicting the thermo-hydraulic behaviour of X-type lattice structures.

2.6. Performance evaluation

Streamline visualization and velocity contour plots were used to observe qualitatively the thermal performance of the configurations considered. The quantitative evaluation was made in terms of the pressure-drop per Unit Length ($\Delta p/L$), the average Nusselt number ($\mathrm{Nu_{avg}}$), and the thermo-hydraulic performance factor (η) for the five α values (40°, 45°, 50°, 55°, and 60°), each with three β values (30°, 36°, and 40°), over $2600 \lesssim \mathrm{Re} \lesssim 8000$ for each configuration.

The thermo-hydraulic performance factor η assesses the combined thermal and hydraulic effectiveness of the investigated lattice configurations by balancing heat transfer enhancement with the pumping power penalty [26,27]. A factor $\eta > 1$ indicates that the heat transfer benefits outweigh the energy lost to increased fluid friction [26,27]. It is defined as follows,

$$\eta = \left(\frac{\mathrm{Nu}}{\mathrm{Nu}_0}\right)\left(\frac{f_0}{f}\right)^{1/3}, \tag{10}$$

where Nu and Nu_0 are the Nusselt numbers of the lattice and smooth channel, respectively, both calculated using Eq. (5), f_0 is the friction factor of the smooth channel, and f is the friction factor of the lattice configuration. Using the same Nusselt-number formulation for both configurations ensures a consistent basis for thermal-hydraulic performance comparison. The friction factor, as defined below, was obtained from the simulated pressure gradient ($\Delta p/L$),

$$f = \left(\frac{2H}{\rho u^2}\right)\left(\frac{\Delta p}{L}\right). \tag{11}$$

Another useful performance evaluation parameter, from a practical application point of view, is the Pumping Power per Unit Length (PP/L), as calculated by

$$\mathrm{PP}/L = \frac{\Delta p}{L} U_{in} A \tag{12}$$

where A is the characteristic cross-sectional area of the X-type lattice channel. As A changes with α, PP/L is different from $\Delta p/L$, although closely relevant.

In the calculations, thermophysical properties were taken from the ANSYS Fluent material database for air at 21.5 °C (c_p = 1006.43 J kg^{-1} K^{-1}, μ = 1.7894 × 10^{-5} Pa s, k = 0.0242 W m^{-1} K^{-1}, Pr = 0.744). This approach follows recent numerical studies on lattice and structured-channel heat transfer [28–30].

3. Results and discussion

A total of 95 numerical simulation runs were carried out. Among them, 75 runs were carried out by varying α with five values (40°, 45°, 50°, 55°, and 60°), each with three β values (30°, 36°, and 40°). For each pair of α-β, five Re values (2645, 3968, 5290, 6613, and 7936, which correspond to the inlet velocity of 4 m/s, 6 m/s, 8 m/s, 10 m/s, and 12 m/s, respectively) are considered. Additionally, 20 more runs were carried out by expanding the range of α (α = 20°, 25°, 30°, and 35°) with the fixed β = 30°, again each with five Re values (2645, 3968, 5290, 6613, and 7936).

Qualitative observations of flow and thermal field characteristics in the considered lattice configures under different Re values are first presented in terms of velocity magnitude contours, streamlines, temperature contours and local Nusselt number (Nu_{loc}). A quantitative analysis of the obtained numerical results is subsequently presented in terms of the average Nusselt number (Nu_{avg}), pressure drop per unit length ($\Delta p/L$), pumping power per unit length (PP/L) and thermal hydraulic performance factor (η), to illustrate quantitatively the individual and combined effects of Re, α and β.

3.1. Qualitative observation of flow and thermal field characteristics

To elucidate the influence of lattice geometry on flow and heat-transfer behaviour, velocity magnitude contours, streamlines, temperature contours and Nu_{loc} are examined firstly for a representative configuration with fixed β = 36° and α = 50° at Re = 5290, as an example. Velocity magnitude and temperature contours are presented on XY-planes at five locations along the streamwise direction (z/L = 0.1, 0.3, 0.5, 0.7, and 0.9, as illustrated in Fig. 8) to highlight the cross-sectional flow and blockage effects induced by the lattice structure, while three-dimensional streamlines along the streamwise direction are presented to illustrate the streamwise flow development and flow redirection through the lattice core. The variation of Nu_{loc} is also presented to illustrate the local heat transfer characteristics along the streamwise direction.

Subsequently, the individual effects of α, β and Re on the flow and thermal field characteristics are observed by varying α between 40° and 60° with fixed β = 36° and Re = 5290, varying β between 30° and 40° with fixed α = 50° and Re = 5290, and varying Re with fixed α = 50° and β = 36°, respectively.

3.1.1. Velocity and thermal field characteristics at fixed α = 50°, β = 36° and Re = 5290

Fig. 9 presents the velocity magnitude and temperature contours on the vertical planes along the streamwise direction at five z/L locations (z/L = 0.1, 0.3, 0.5, 0.7, and 0.9) for fixed α = 50°, β = 36° and Re = 5290. At the upstream location, the incoming fluid accelerates as it passes through the constricted passages formed by the inclined lattice members. High-velocity regions are concentrated within the main flow channels, whereas lower velocities occur near the strut surfaces due to viscous effects. The strong velocity gradients adjacent to the solid boundaries indicate the development of boundary layers along the lattice members. As the flow progresses downstream, it is repeatedly redirected by the inclined struts, producing localized acceleration zones and reduced-velocity regions immediately behind the solid members. These low-velocity zones correspond to wake structures generated by flow separation. The temperature contours in the figure show the corresponding thermal development. The fluid enters the lattice at a lower temperature and is progressively warmed along the flow direction as heat is transferred from the heated base. Higher temperatures are observed near the heated wall and around the solid members, while relatively cooler fluid is retained within the main flow passages. As the flow advances downstream, thermal diffusion and mixing spread the heated region farther into the core, indicating progressive thermal development within the lattice.

The visualization of the corresponding streamlines presented in Fig. 10 further clarifies the internal flow paths. The streamlines remain predominantly aligned with the main flow direction, but repeated deflection around the inclined struts gives rise to localized recirculation downstream of each member. These secondary flow structures promote momentum exchange between the core flow and the near-wall fluid, thereby enhancing fluid mixing within the lattice. The repeated sequence of acceleration, deflection, and wake formation across successive unit cells governs the overall hydrodynamic development of the flow.

The results presented in Fig. 11 provide the variation of the convective heat transfer, in terms of Nu_{loc}, along the streamwise direction. It is seen that Nu_{loc} decreases monotonically along the streamwise direction with gradually reducing rates. This behaviour indicates strong heat transfer near the inlet, where the thermal boundary layer is relatively thin and the incoming fluid is still comparatively cool. As the fluid flows downstream, the thermal boundary layer develops and the fluid temperature rises, reducing the local temperature difference that drives convection and thereby lowering Nu_{loc}. The gradual levelling of the curve farther downstream suggests that the local heat transfer process approaches a more thermally developed condition.

In summary, the combined results of velocity, streamline, temperature, and local Nusselt number demonstrate that the inclined lattice members induce repeated flow acceleration, deflection, wake formation, and thermal mixing within each unit cell. These mechanisms disrupt the thermal boundary layer near the entrance and sustain convective transport along the lattice, thereby governing the overall heat transfer behaviour of the α50°-β36° lattice configuration.

3.1.2. Effect of Reynolds number

At the fixed configuration (α = 50° and β = 36°), the influence of Reynolds number on the flow and thermal fields is examined using velocity magnitude and temperature distributions, streamline visualizations, and local Nusselt number variation. The results of the velocity magnitude contours presented in Fig. 12 (left column) show that as Re increases, the high-velocity core progressively expands within the central flow passage, while the low-velocity regions adjacent to the strut surfaces become more confined. This indicates stronger inertial effects and enhanced flow acceleration through the constricted lattice passage. The temperature contours presented in Fig. 12 (right column) show that at low Reynolds numbers, the heated region extends farther from the heated walls into the fluid domain, indicating weaker convective removal of heat. As Reynolds number increases, cooler fluid penetrates more effectively into the lattice core, and the high-temperature region becomes increasingly confined near the heated surfaces and around the strut, reflecting the progressive thinning of the thermal boundary layer and improved heat extraction.

The streamline visualizations presented in Fig. 13 further show that the flow is redirected around the inclined struts at all Reynolds numbers, but the degree of streamline curvature and local recirculation become more pronounced as Re increases. At lower Reynolds numbers, the flow follows smoother paths with weaker local separation, whereas higher Reynolds numbers promote stronger flow deflection and more evident secondary re-circulatory structures near the struts. These features enhance momentum exchange between the core flow and the near-wall fluid.

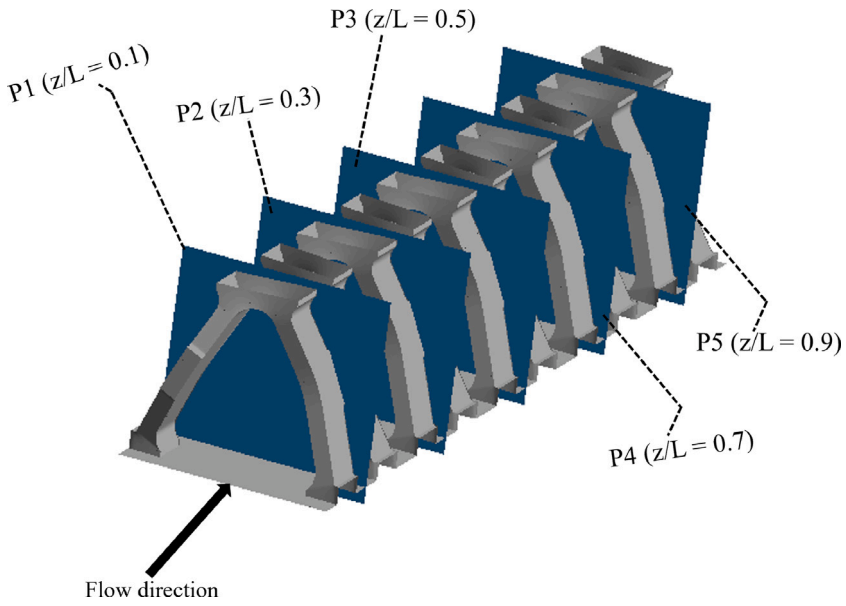


Fig. 8. Schematic illustration of the streamwise cross-sectional planes used for velocity and temperature contour visualization at different normalized axial locations (z/L) within the X-type lattice structure.

The behaviour described above is quantitatively confirmed by the variation of the local Nusselt number with Re as presented in Fig. 14, where it is seen that higher Reynolds numbers consistently produce larger Nu_{loc} values at the five streamwise locations. For each Reynolds number, Nu_{loc} decreases with increasing z/L, indicating strong entrance heat transfer followed by progressive thermal development downstream which reduces heat transfer. The results further show that heat transfer is significantly improved when Re increases, due to stronger flow acceleration, enhanced flow redirection and mixing, and progressive thinning of the thermal boundary layer within the lattice structure.

3.1.3. Effect of α

At the fixed $\beta = 36°$ and Re = 5290, the influence of the curvature angle α on the flow and thermal fields is also examined using velocity magnitude and temperature distributions, streamline visualizations and local Nusselt number variation. The velocity magnitude contours and corresponding temperature fields on the vertical plane at $z/L = 0.5$ are presented in Fig. 15 for five α values ranging from 40° to 60° for the fixed $\beta = 36°$ and Re = 5290. From the results, it is observed that as α increases, the flow structure becomes progressively more aligned with the streamwise direction. At lower inclination angles ($\alpha = 40°–45°$), the inclined struts impose stronger geometric obstruction, leading to accelerated flow through constricted passages and enhanced lateral deflection. This results in localized low-velocity regions near the strut surfaces and stronger velocity gradients across the flow domain. In contrast, at higher inclination angles ($\alpha = 55°–60°$), the flow encounters reduced geometric resistance, producing a more uniform high-velocity core with diminished flow separation and weaker velocity gradients.

The streamline visualizations (Fig. 16), further highlight this transition in flow behaviour. At lower α, the flow is strongly redirected around the inclined struts, generating pronounced curvature and localized recirculation zones. These features promote enhanced mixing between the core flow and near-wall fluid. As α increases, the streamlines become progressively straighter, indicating reduced flow deflection and weaker secondary flow structures. This reflects a transition from mixing-dominated transport to convection governed by streamlined flow.

The temperature contours exhibit a corresponding dependence on α. At lower inclination angles, stronger flow redirection enhances convective interaction near the heated surfaces, resulting in steeper temperature gradients near the heated surfaces and enhanced convective heat transfer. Conversely, at higher α, the reduced mixing leads to smoother temperature fields with weaker thermal gradients, indicating reduced convective heat transfer despite improved fluid penetration into the lattice core.

These observations are quantitatively confirmed by the local Nusselt number distributions shown in Fig. 17. For all α values considered, Nu_{loc} decreases with increasing z/L, reflecting thermal development along the flow direction. More importantly, Nu_{loc} consistently decreases with increasing α, with the highest value observed at $\alpha = 40°$ and the lowest value $\alpha = 60°$. This confirms that lower inclination angles enhance convective heat transfer through intensified flow redirection, mixing, and boundary-layer disruption.

Overall, the inclination angle α governs a fundamental trade-off between flow resistance and thermal performance. Lower α enhances heat transfer through stronger flow disruption and mixing, whereas higher α promotes smoother flow with potentially reduced pressure losses but diminished convective heat transfer. This highlights the critical role of geometric orientation in balancing thermal enhancement and hydraulic efficiency in lattice structures.

3.1.4. Effect of β

At the fixed $\alpha = 50°$ and Re = 5290, the influence of β on the flow and thermal fields is examined, again using velocity contours, temperature distributions, streamline visualizations, and local Nusselt number distributions. The velocity magnitude contours presented in Fig. 18 clearly show that varying β from 30° to 40° produces much smaller changes in the flow field relative to those observed for varying α. Similarly, the temperature contours presented in this figure also exhibit very small changes in the thermal fields. The variation in β only leads to very slight redistribution of the heated region around the inclined strut and lower heated wall, but does not fundamentally alters the overall thermal structure of the flow. This suggests that changing β primarily modifies slightly the local flow redistribution and near-wall convective interaction, rather than fundamentally alters the global heat-transfer mechanism. The streamline visualizations presented in Fig. 19 support these observations. Although it can be seen that for $\beta = 30°$, the flow undergoes slightly stronger local redirection and recirculation around the lattice members and increasing β gradually, but only very slightly relaxes these features and produces a somewhat smoother streamwise development, nevertheless, the overall streamline topology basically remains similar across the three β values, indicating

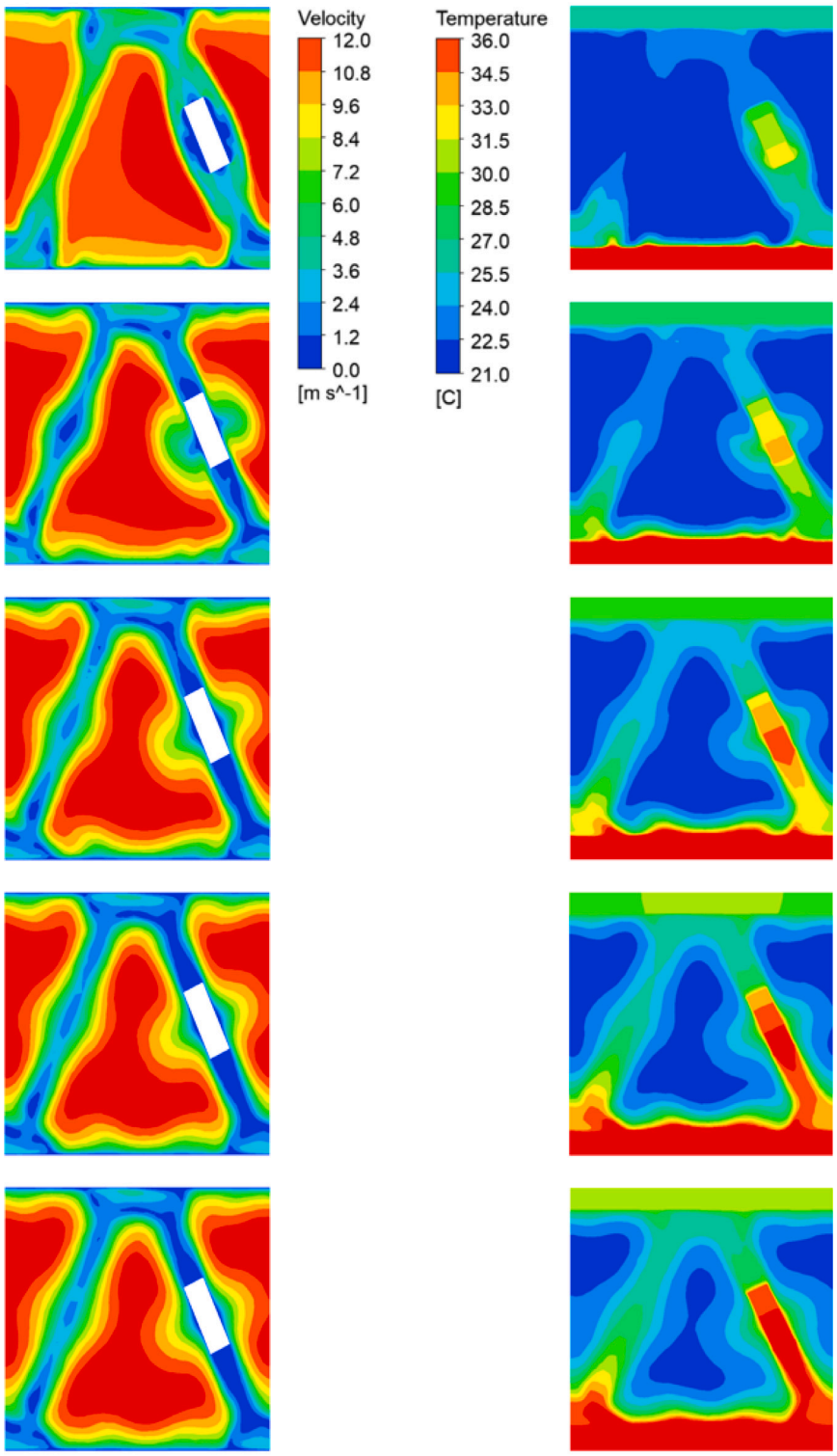


Fig. 9. Velocity Magnitude contours (left column) and temperature contours (right column) on the vertical plane along the streamwise direction at different z/L positions for fixed $\alpha = 50°$, $\beta = 36°$ and Re = 5290: $z/L = 0.1$ (first row), $z/L = 0.3$ (second row), $z/L = 0.5$ (third row), $z/L = 0.7$ (fourth row), and $z/L = 0.9$ (fifth row).

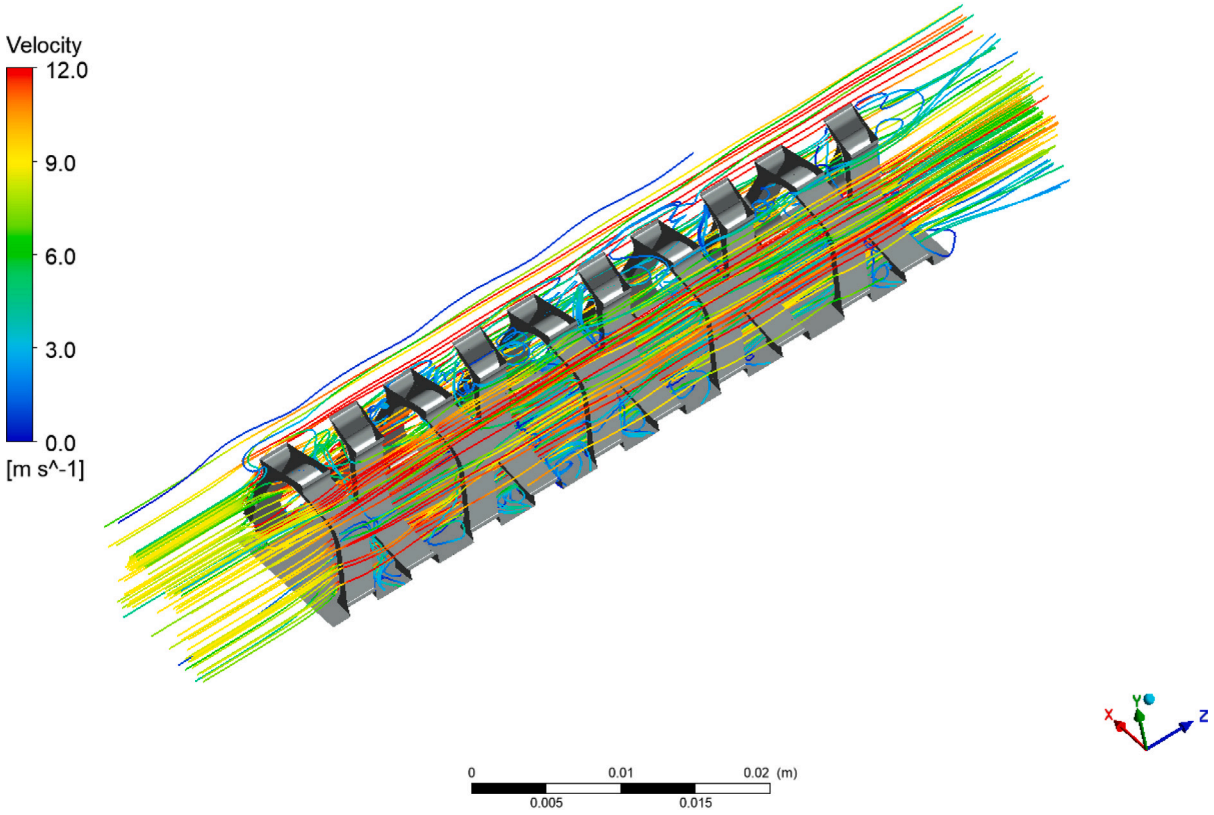


Fig. 10. Streamlines along the streamwise direction.

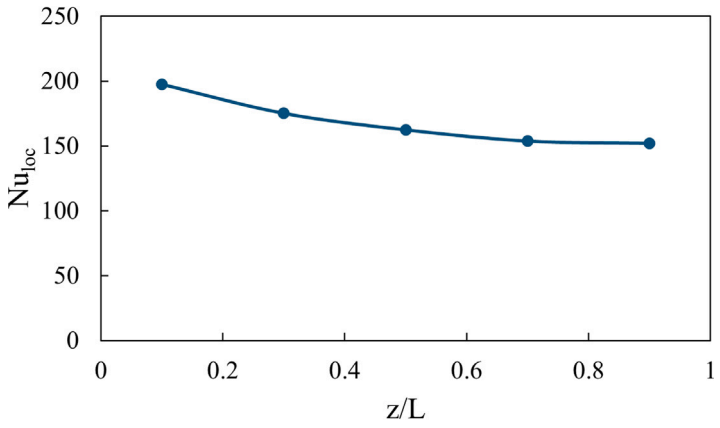


Fig. 11. Variation of the local Nusselt number along the streamwise direction for the case of $\alpha = 50°$, $\beta = 36°$, and $Re = 5290$.

that the effect of β is marginal compared with the much stronger geometric influence of α.

These observations are quantitatively confirmed by the local Nusselt number distributions, as shown in Fig. 20. For all three β values, Nu_{loc} decreases along the streamwise direction. However, the very small differences among the three β configurations remain very small, indicating that the influence of β on Nu_{loc} is very weak under.

3.2. Quantitative analysis

3.2.1. Convective heat transfer (Nu_{avg})

Fig. 21 presents the average Nusselt number (Nu_{avg}) plotted against Re for all lattice configurations considered. It shows that for all configurations, Nu_{avg} increases monotonically with Re. This agrees with the expected characteristics of forced convection in complex internal passages, where increasing Re enhances inertial effects, promotes flow instability and mixing, and leads to progressive thinning of the thermal boundary layer, thereby strengthening convective heat transfer. Similar results have also been reported for strut-based lattice heat-transfer structures by Aider and Singh. [31] and Ho et al. [16], who attributed the increase in Nu_{avg} to intensified flow acceleration and fluid–solid interaction at higher Reynolds numbers.

Reducing the α values reveals that the sensitivity of Nu_{avg} to α is not uniform across the range of α investigated, as shown in Fig. 21. While the Nu_{avg}-Re curves for $\alpha = 50°$–$60°$ remain relatively close to one another, progressively larger separations are observed as α decreases below 40°. Relative to $\alpha = 40°$, the average Nusselt number increases by ≈13%, 24%, and 35% for $\alpha = 30°$, 25°, and 20°, respectively, across the investigated Reynolds-number range. This enhancement indicates that saturation behaviour is not yet evident within the investigated

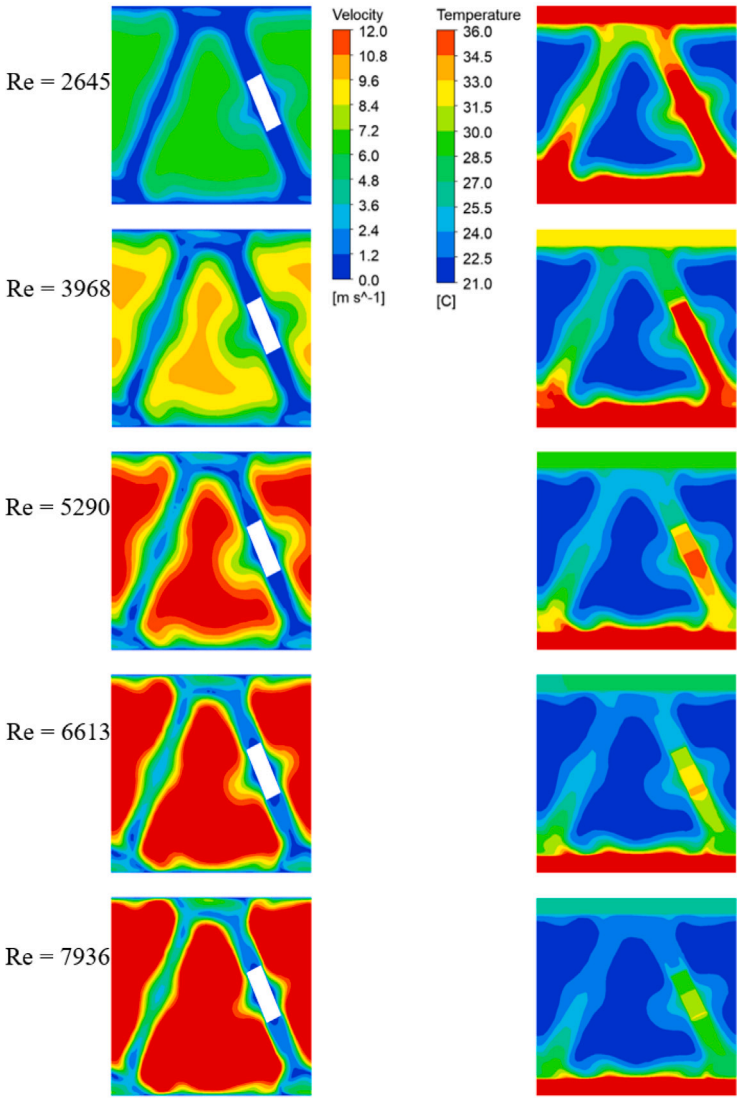


Fig. 12. Velocity Magnitude contours (left column) and temperature contours (right column) on the vertical plane at $z/L = 0.5$ at different Re values for fixed $\alpha = 50°$ and $\beta = 36°$.

α range. The improved performance is attributed to stronger geometric confinement, increased flow acceleration through the narrowed inter-strut passages, and enhanced near-wall velocity gradients, which promote more effective thermal-boundary-layer disruption and fluid–surface interaction. Similar heat-transfer enhancement with increased geometric confinement (e.g., reduced lattice pitch/spacing) has also been reported by Park et al. [32]. Consequently, the enhancement observed between $\alpha = 40°$ and $20°$ (≈35%) is substantially larger than that observed between $\alpha = 60°$ and $40°$ (≈20%). This indicates a reduced sensitivity of convective heat transfer to α once the flow passages become sufficiently open. In this regime, further widening of the lattice channels weakens flow acceleration and reduces the intensity of near-wall velocity gradients, resulting in diminishing returns in heat-transfer enhancement despite continued increases in Reynolds number. Similar saturation behaviour has been reported in strut-based lattice heat sinks, where increasing lattice openness beyond a critical level produces only marginal improvements in Nusselt number due to weakened flow acceleration and reduced vortex intensity [14,33].

A comparison of the results between $\beta = 30°$ and $\beta = 36°$ reveals that the influence of β on the Nusselt number is modest and non-monotonic, with the effect depending on both α and Re. For certain configurations (e.g., $\alpha = 40°$ at higher Re and $\alpha = 55°$ at intermediate Re), $\beta = 36°$ yields slightly higher Nu_{avg} than $\beta = 30°$. This can be attributed to enhanced lateral flow redirection and the onset of secondary-flow motion induced by the increased inclination, which promotes fluid mixing and disrupt thermal boundary layers. Similar trends have also been reported in strut-based lattice heat sinks, where inclination-induced secondary flows and spiral structures provide localized heat-transfer enhancement without producing a monotonic trend across Re [33,34]. However, for other configurations, $\beta = 30°$ consistently leads higher Nu_{avg} than $\beta = 36°$. In these cases, increasing β further reduces flow confinement and weakens flow impingement on the strut surfaces, diminishing the effectiveness of convective heat transfer. This competing effect between mixing enhancement and loss of confinement underpins the observed non-monotonic dependence of Nu_{avg} on β. Further increasing β to 40° (Fig. 21(c)) does not result in systematic heat-transfer enhancement and, in several cases, leads to Nu_{avg} comparable to or slightly lower than those obtained at $\beta = 36°$ (Fig. 21(b)). This suggests that excessive inclination reduces the intensity of flow-surface interaction, as the flow increasingly bypasses the strut surfaces rather than impinging upon them.

Overall, the results demonstrate that both Re and α strongly influence convective heat transfer within the X-type lattice structure. While increasing Re enhances heat transfer through greater inertial transport

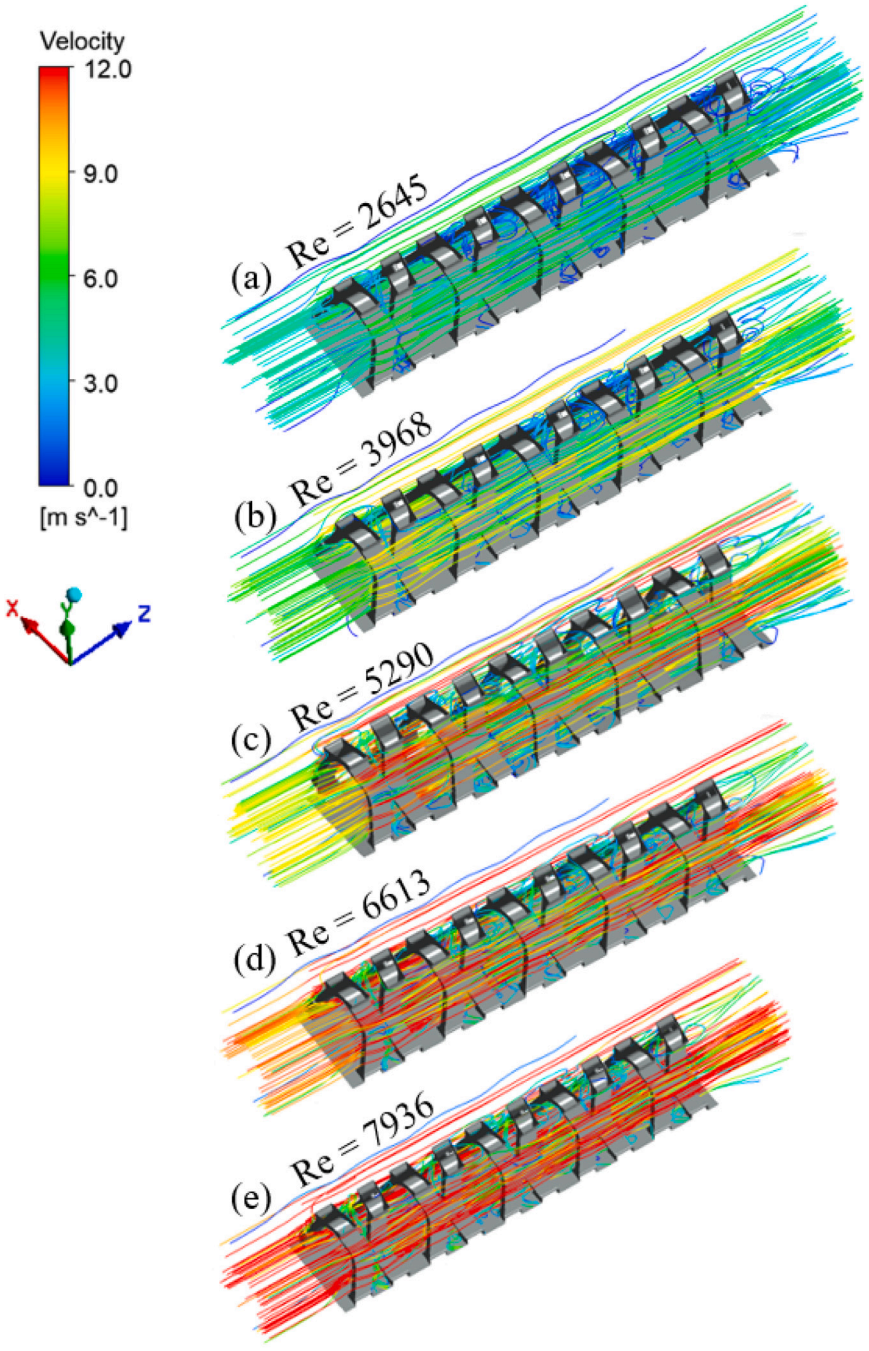


Fig. 13. Streamlines along the streamwise direction at different Re values for fixed $\alpha = 50°$ and $\beta = 36°$.

and boundary-layer thinning, variations in α directly modify the degree of flow confinement and fluid–surface interaction. In contrast, the influence of β remains comparatively weaker and non-monotonic. These observations identify α as the dominant geometric parameter governing convective heat-transfer performance within the investigated design space, whereas variations in β produce comparatively smaller and non-monotonic changes. The results therefore indicate that optimization efforts should primarily focus on α, with β serving as a secondary tuning parameter for refining flow mixing and heat-transfer behaviour.

To quantify the combined effect of Re, α and β on Nu_{avg}, a multivariable regression analysis was performed using the obtained data from all simulation runs. The result is presented in Fig. 22(a), which shows that the following correlation can be established between Nu_{avg} and the combination of Re, α and β in the form of $Re^a \alpha^b \beta^c$,

$$Nu_{avg} = 2.1661 Re^{0.733} \alpha^{-0.482} \beta^{-0.011} + 0.7451, \quad (13)$$

in which $a = 0.733$, $b = -0.482$, and $c = -0.011$, respectively. It is seen that the numerical results collapse onto this best-fitting straight line represented by the above correlation, with the regression constant of $R^2 = 0.9984$. From the correlation, it is clear that the effects of Re and α in Nu_{avg} are significant (with $a = 0.733$ and $b = -0.482$, respectively), with convective heat transfer increasing strongly with flow rate, whereas larger strut angle reducing the effective heat-transfer enhancement within the lattice. However, the effect of β is very weak (with $c = -0.011$). This is further shown by the following correlation between Nu_{avg} and the combination of Re and α only, with the exclusion

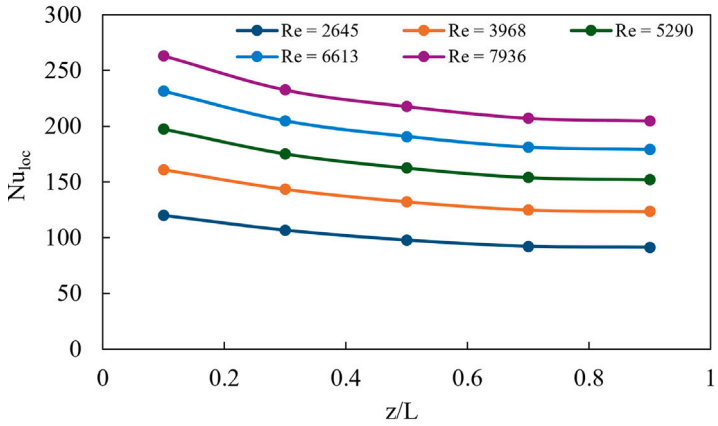


Fig. 14. Local Nusselt number Nu_{loc} along the streamwise direction at different Re values for fixed $\alpha = 50°$ and $\beta = 36°$.

of β, in the form of $Re^a\alpha^b$,

$$Nu_{avg} = 2.1Re^{0.733}\alpha^{-0.484} + 0.7383, \quad (14)$$

in which $a = 0.733$ and $b = -0.484$, respectively. As shown in Fig. 22(b), it can be observed that the numerical results also collapse onto this best-fitting straight line represented by this correlation, with the regression constant of $R^2 = 0.9966$ and no change or very small changes of the exponents, coefficients and constants of both correlations above. All these results agree with the trends showing in Fig. 21.

3.2.2. Pressure drop per unit length ($\Delta p/L$)

Fig. 23 presents the pressure drop per unit length ($\Delta p/L$) plotted against Re for all lattice configurations considered. The results show that, similar to that for Nu_{avg}, $\Delta p/L$ increases monotonically and substantially with the Reynolds number, clearly reflecting the growing dominance of inertial effects as the flow rate increases. At a fixed α angle, increasing Reynolds number results in a progressively steeper rise in $\Delta p/L$, indicating a transition from predominantly viscous losses at lower Reynolds numbers to inertia-dominated losses at higher Reynolds numbers. This nonlinear pressure–velocity relationship is characteristic of periodic lattice structures and arises from intensified flow separation and interaction between wakes generated by successive unit cells, as also reported by Kaur et al. [35], who demonstrated that wake interference and form drag in additively manufactured lattice frames become increasingly dominant contributors to pressure loss with increasing Reynolds number.

For a fixed β angle, decreasing the α angle consistently results in higher $\Delta p/L$ across the entire Reynolds number range. This behaviour is attributable to geometric confinement within the lattice core: smaller α angles reduce the effective hydraulic opening between successive struts, leading to flow acceleration, increased local shear, and enhanced form drag. Consequently, greater momentum losses accumulate along the flow direction. A similar trend was observed by Bernardini et al. [36], who showed that variations in lattice geometry at identical Reynolds numbers lead to systematic changes in pressure loss due to altered flow confinement and wake interactions.

From the above figure, it is seen that at fixed α and Reynolds number, the influence of β on the $\Delta p/L$ is found to be similarly modest and strongly Re dependent. At the lowest Reynolds number investigated, configurations with $\beta = 30°$ (Fig. 23(a)), exhibit slightly higher $\Delta p/L$ than those with $\beta = 36°$ (Fig. 23(b)) and $\beta = 40°$ (Fig. 23(c)), for several α values. As Re increases, this ordering reverses, and $\Delta p/L$ increases systematically with β, following the trend ($\beta = 40°$) > ($\beta = 36°$) > ($\beta = 30°$). This behaviour indicates a transition from viscous-dominated resistance at low Reynolds numbers, where permeability effects primarily govern pressure losses to inertia-dominated resistance at higher Reynolds numbers, where enhanced flow redirection and form drag associated with larger β angles become increasingly significant, as also reported by Aghaei-Jouybari et al. [37] who showed that orientation-dependent flow deflection, driven by inertia, separation and wake dynamics, becomes increasingly important as Reynolds number increases.

Overall, the above results demonstrate that while Re remains the dominant parameter controlling $\Delta p/L$, the effect of α is also significant. Nevertheless the effect of β is very small. These quantitative results agree very well with the qualitative observations. The combined effects of Re, α and β are further demonstrated by the quantitative results shown in Fig. 24, which shows that the following correlation between $\Delta p/L$ and the combination of Re, α and β in the form of $Re^a\alpha^b\beta^c$ can be established through a multi-variable regression analysis using the obtained data from all simulation runs,

$$\Delta p/L = 0.0021Re^{1.942}\alpha^{-0.869}\beta^{0.001} - 5.137, \quad (15)$$

in which $a = 1.942$, $b = -0.869$, and $c = 0.001$, respectively. It is seen that the numerical results collapse onto this best-fitting straight line represented by the above correlation, with the regression constant of $R^2 = 0.9984$. Similarly, the effect of β is very weak (with $c = -0.001$). This is further shown by the following correlation between $\Delta p/L$ and the combination of Re and α only, with the exclusion of β, in the form of $Re^a\alpha^b$,

$$\Delta p/L = 0.0021Re^{1.944}\alpha^{-0.869} - 4.8367, \quad (16)$$

in which $a = 1.944$ and $b = -0.869$, respectively. As shown in Fig. 24(b), it can be observed that the numerical results also collapse onto this best-fitting straight line represented by this correlation, with the regression constant of $R^2 = 0.999$ and no change or very small changes of the exponents, coefficients and constants of both correlations above.

3.2.3. Pumping power per unit length (PP/L)

Fig. 25 presents the pumping power per unit length (PP/L) plotted against Re for all lattice configurations considered. The results show that, similar to that for $\Delta p/L$, PP/L increases monotonically and substantially with the Reynolds number, clearly reflecting the growing dominance of inertial effects as the flow rate increases. The very similar features to $\Delta p/L$ when Re, α, and β change are due to the close relevance between PP/L and $\Delta p/L$, as shown in Eq. (12), although the extra role played by α makes them significantly different, particularly quantitatively.

Similarly, the combined effects of Re, α and β on PP_L can be demonstrated by the quantitative results shown in Fig. 26, which shows that the following correlation between PP/L and the combination of Re, α and β in the form of $Re^a\alpha^b\beta^c$ can be established through a multi-variable regression analysis using the obtained data from all simulation runs,

$$PP/L = 3.606 \times 10^{-11}Re^{2.942}\alpha^{-0.284}\beta^{0.005} - 8.123 \times 10^{-3}, \quad (17)$$

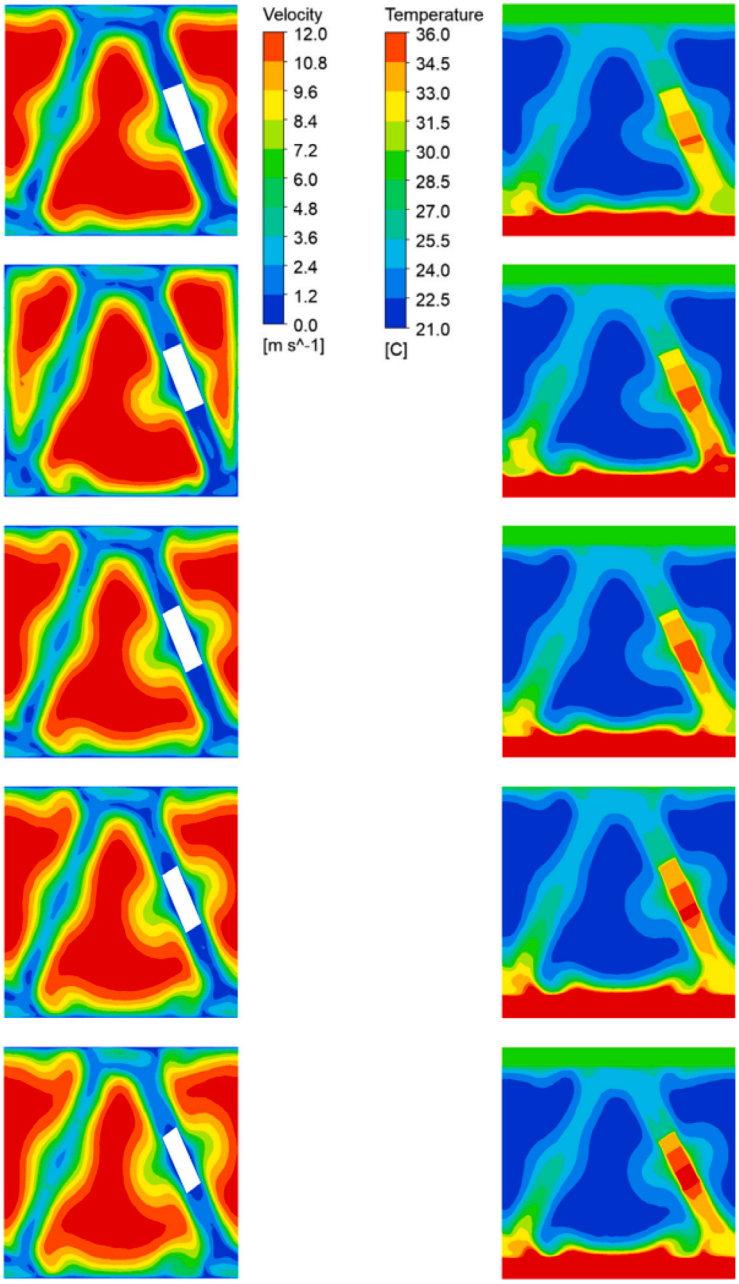


Fig. 15. Velocity Magnitude contours (left column) and temperature contours (right column) on the vertical plane at $z/L = 0.5$ at different α values for fixed $\beta = 36°$ and Re = 5290: $\alpha = 40°$ (first row), $\alpha = 45°$ (second row), $\alpha = 50°$ (third row), $\alpha = 55°$ (fourth row), and $\alpha = 60°$ (fifth row).

in which $a = 2.942$, $b = -0.284$, and $c = 0.005$, respectively. It is seen that the numerical results collapse closely onto this best-fitting straight line represented by the above correlation, with the regression constant of $R^2 = 0.9984$. Again it is seen that the effect of β is very weak (with $c = 0.005$). This is further shown by the following correlation between PP/L and the combination of Re and α only, with the exclusion of β, in the form of $Re^a\alpha^b$,

$$PP/L = 3.555 \times 10^{-11} Re^{2.942} \alpha^{-0.285} - 8.139 \times 10^{-3}, \quad (18)$$

in which $a = 2.942$ and $b = -0.285$, respectively. As shown in Fig. 26(b), it can be observed that the numerical results also collapse onto this best-fitting straight line represented by this correlation, with the regression constant of $R^2 = 0.9982$ and no change or very small changes of the exponents, coefficients and constants of both correlations above.

3.2.4. Thermal hydraulic performance factor (η)

The calculated thermal hydraulic performance factor (η) values from the simulated results are plotted against Re in Fig. 27 for all α-β configurations considered. The performance factor simultaneously accounts for convective heat-transfer enhancement and the associated pressure-drop penalty, providing a balanced metric for practical design assessment. A larger values of η indicates a better overall performance.

The results in the figure show that across all configurations, η decreases monotonically and substantially with increasing Reynolds number. Although the average Nusselt number increases with Re, the corresponding rise in pressure drop is more pronounced, resulting in a gradual deterioration of thermal-hydraulic efficiency at higher flow rates. Similar Re-dependent reductions in performance factor have been widely reported for structured channels and lattice-based heat sinks (e.g., [38]), where inertial losses increase more rapidly than heat-transfer gains.

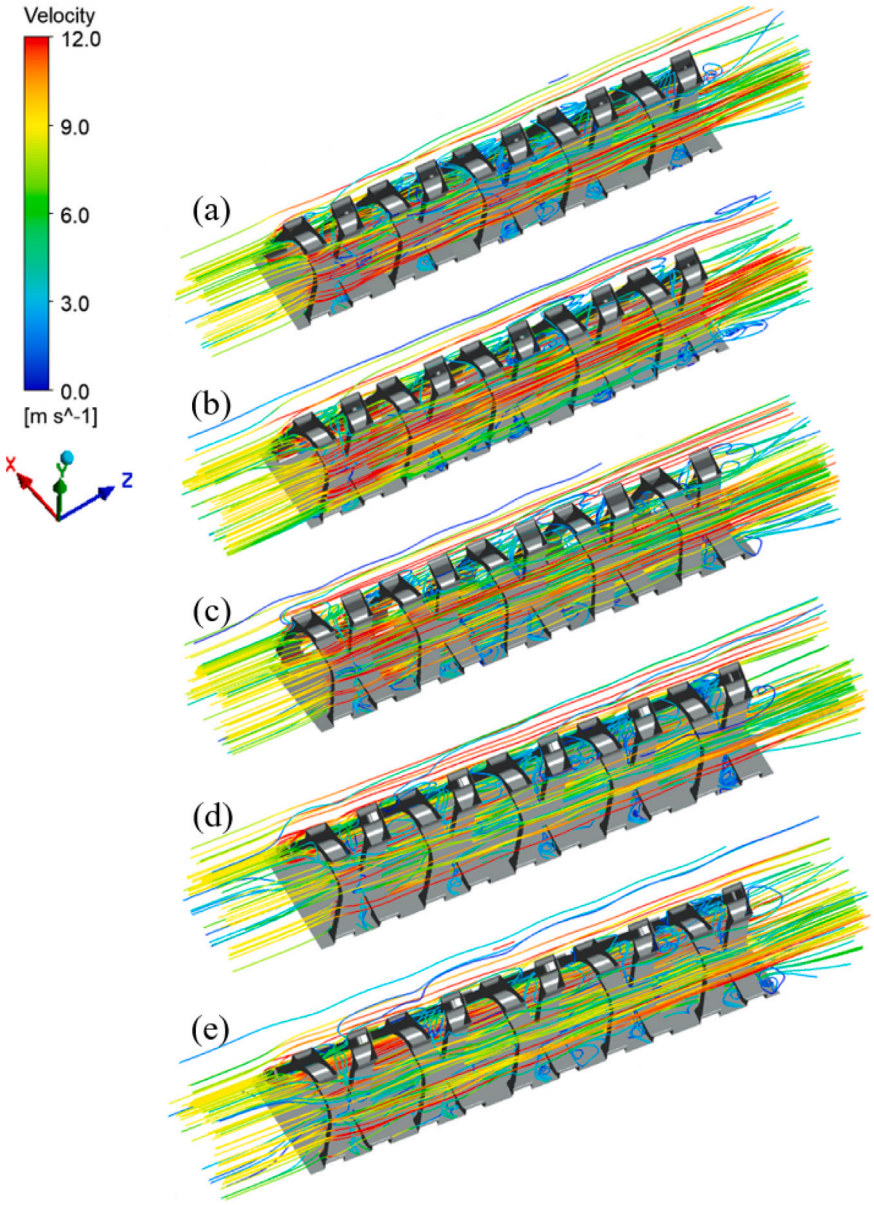


Fig. 16. Streamlines along the streamwise direction at different α values for fixed $\beta = 36°$ and Re = 5290: (a) $\alpha = 40°$, (b) $\alpha = 45°$, (c) $\alpha = 50°$, (d) $\alpha = 55°$, and (e) $\alpha = 60°$.

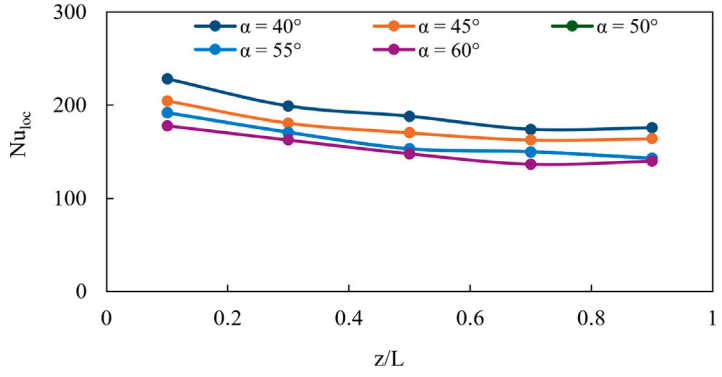


Fig. 17. Local Nusselt number Nu_{loc} along the streamwise direction at different α values for the fixed $\beta = 36°$ and Re = 5290.

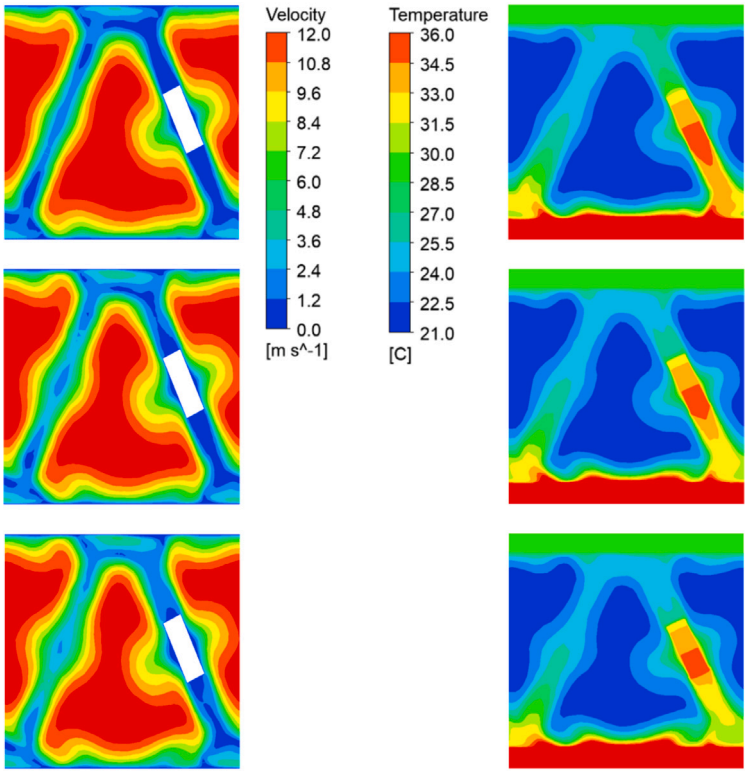


Fig. 18. Velocity Magnitude contours (left column) and temperature contours (right column) on the vertical plane at $z/L = 0.5$ at different β values for fixed $\alpha = 50°$ and Re = 5290: $\beta = 30°$ (first row), $\beta = 36°$ (second row), and $\beta = 40°$ (third row).

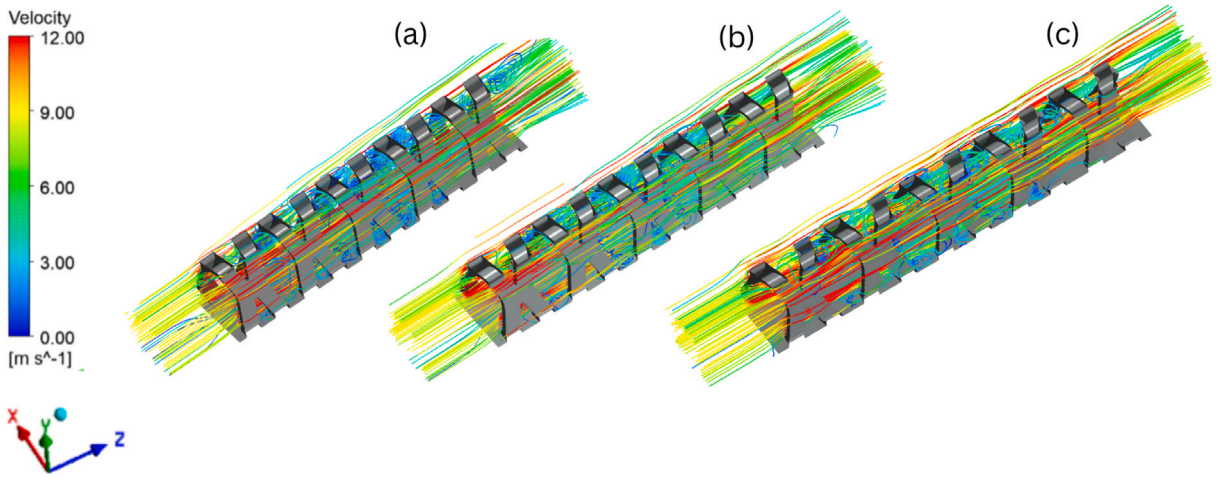


Fig. 19. Streamlines along the streamwise direction at different β values for fixed $\alpha = 50°$ and Re = 5290: (a) $\beta = 30°$; (b) $\beta = 36°$, and (c) $\beta = 40°$.

For a fixed β angle, decreasing the α angle consistently yields higher thermal-hydraulic performance across the entire Re range, showing its significant effect on η. As elaborated above, this behaviour reflects the dominant role of geometric confinement; smaller α angles enhance convective heat transfer through stronger flow acceleration and intensified fluid–solid interaction, while the associated increase in pressure drop remains proportionally lower than the corresponding heat-transfer gain. As α increases, widening of the flow passages weakens heat-transfer enhancement, while pressure losses remain significant, resulting in a net decline in thermal-hydraulic performance.

The results also show that the influence of β on the performance factor, similar to that on the average Nusselt number and pressure drop, is very marginally, compared to that of α. It is found that for a given α, the η-Re curves corresponding to $\beta = 30°$, 36°, and 40° remain closely grouped. At $Re \approx 4000$ and $\alpha = 45°$, η for $\beta = 40°$ is approximately 2% lower than that for $\beta = 30°$, while the difference between $\beta = 30°$ and $\beta = 36°$ remains within 1%. As Re increases, the gaps between the β-dependent curves diminish further, further implying that β primarily modulates the balance between heat-transfer enhancement and pressure-drop penalty rather than fundamentally altering the overall performance trend.

A similar multi-variable regression analysis was performed to show quantitatively the combined effects of Re, α and β on η in the form of $\mathrm{Re}^a\alpha^b\beta^c$ using the obtained data from all simulation runs, and the following quadratic correlation can be established,

$$\eta = -145.91x^2 + 61.14x - 3.6691 \tag{19}$$

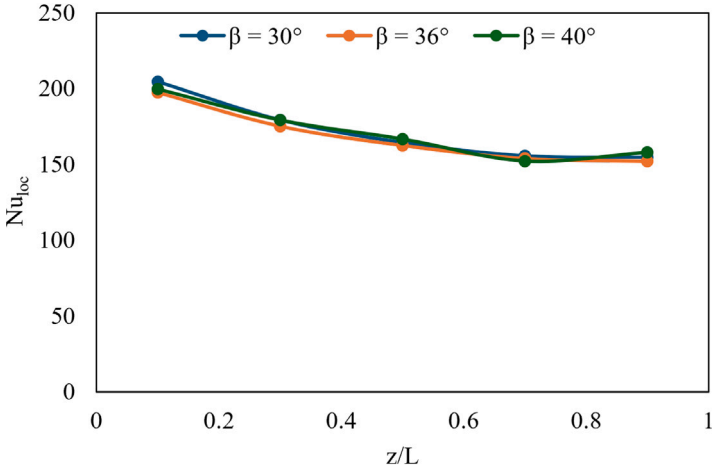


Fig. 20. Local Nusselt number Nu_{loc} along the streamwise direction at different β values for fixed $\alpha = 50°$ and Re = 5290.

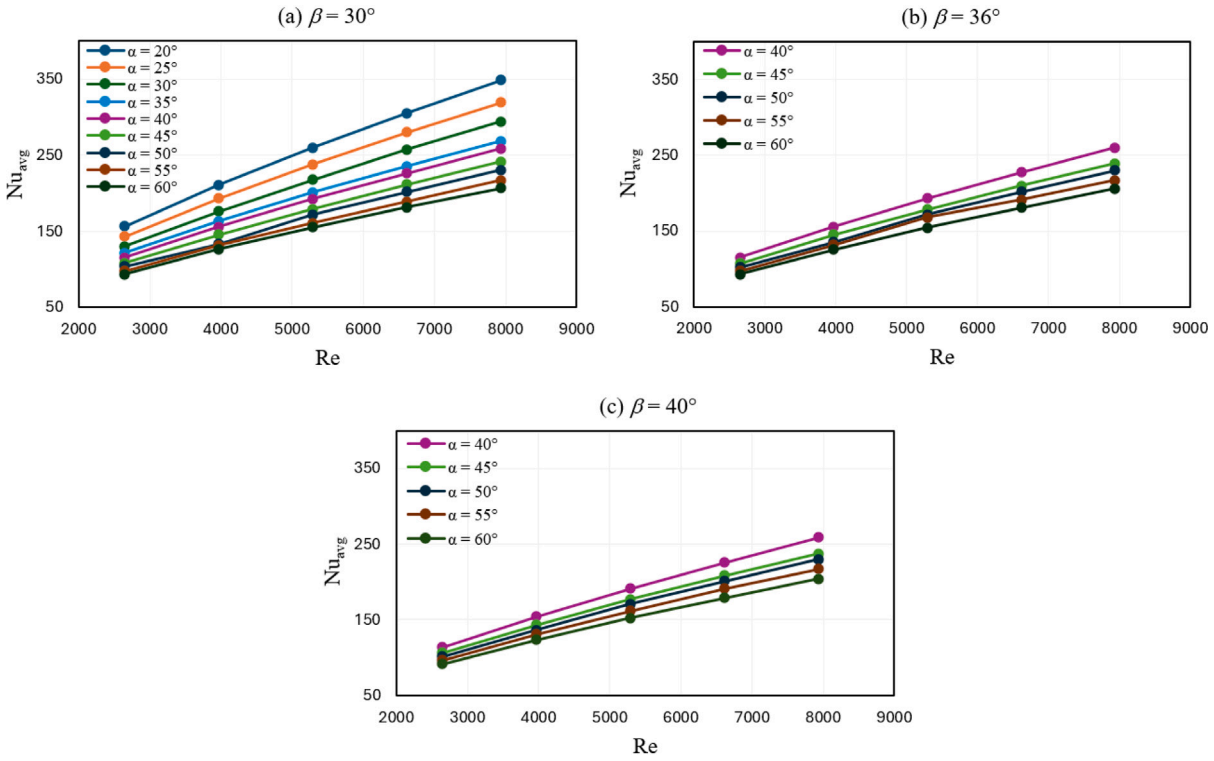


Fig. 21. Nu_{avg} plotted against Re for different lattice configurations: (a) $\beta = 30°$, (b) $\beta = 36°$, and (c) $\beta = 40°$, respectively.

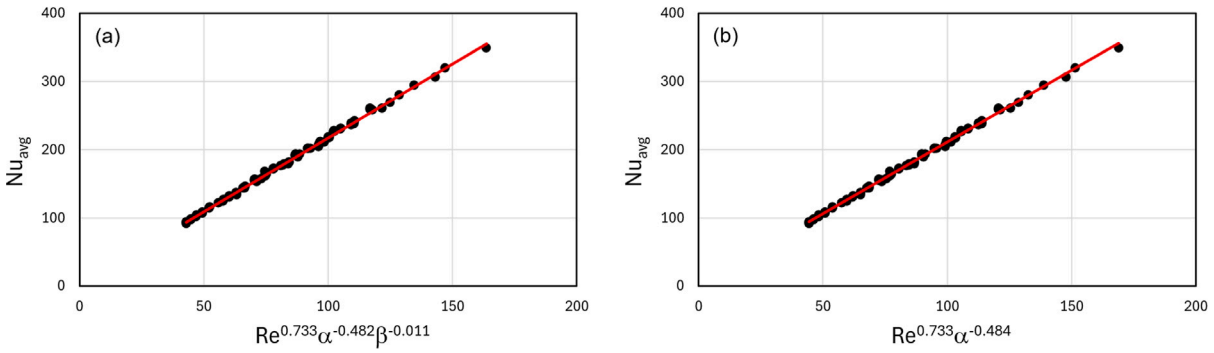


Fig. 22. (a) The correlation between Nu_{avg} and $Re^{0.733}\alpha^{-0.482}\beta^{-0.011}$ and (b) the correlation between Nu_{avg} and $Re^{0.733}\alpha^{-0.484}$, with the solid lines representing the best-fitting straight lines obtained through a multi-variable regress analysis using the obtained data from all simulation runs.

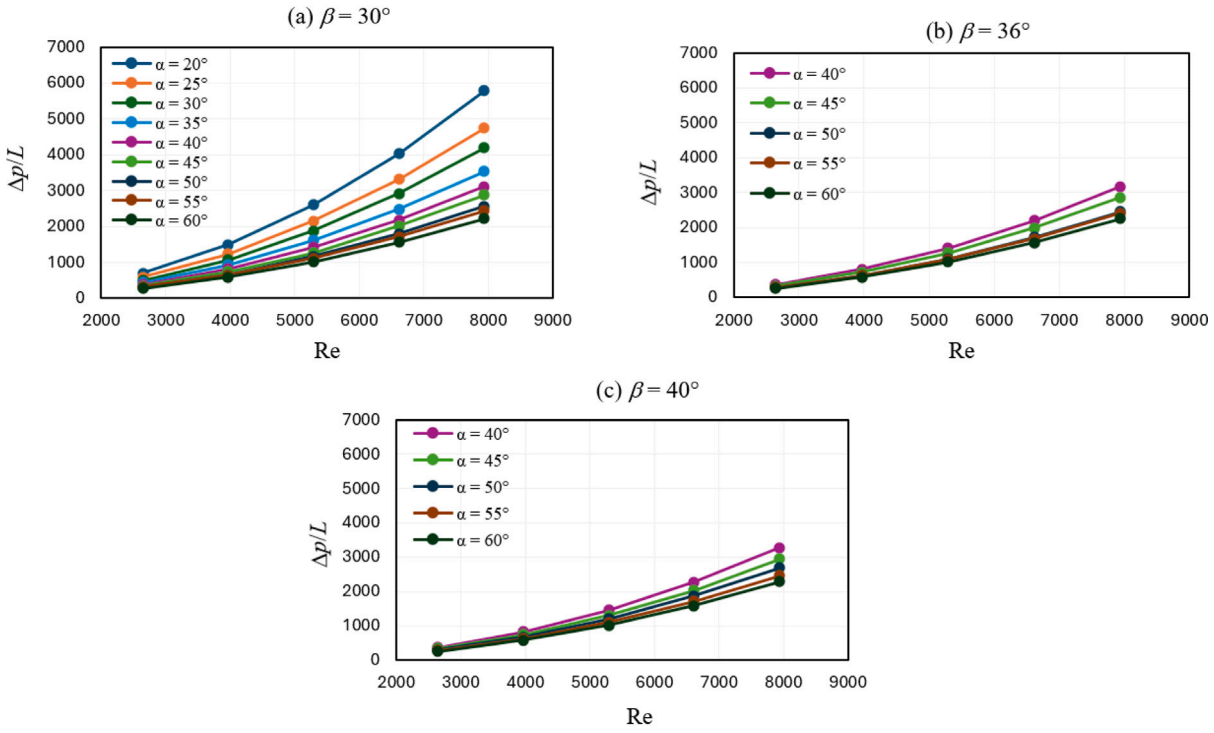


Fig. 23. $\Delta p/L$ plotted against Re for different lattice configurations: (a) β = 30°, (b) β = 36°, and (c) β = 40°, respectively.

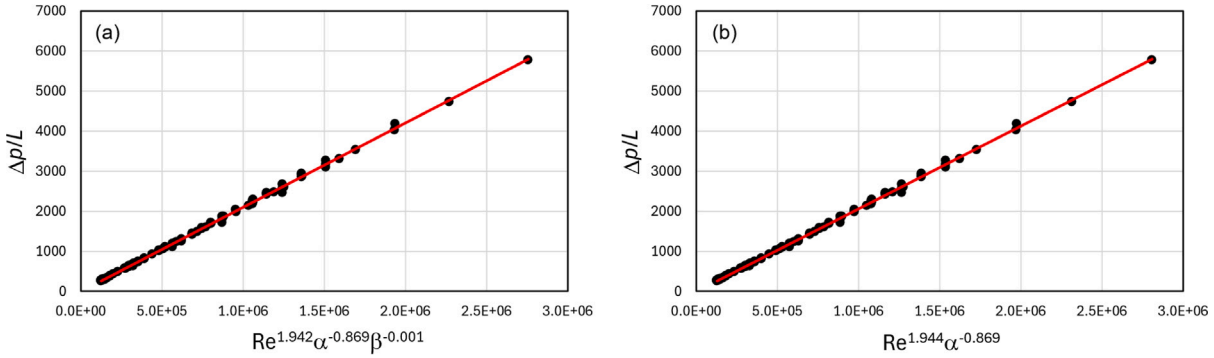


Fig. 24. (a) The correlation between $\Delta p/L$ and $\mathrm{Re}^{1.942}\alpha^{-0.869}\beta^{-0.001}$ and (b) the correlation between $\Delta p/L$ and $\mathrm{Re}^{1.944}\alpha^{-0.869}$, with the solid lines representing the best-fitting straight lines obtained through a multi-variable regress analysis using the obtained data from all simulation runs.

in which $x = \mathrm{Re}^{-0.104}\alpha^{-0.227}\beta^{-0.038}$, with $a = -0.104$, $b = -0.227$, and $c = 0.038$, respectively. It is seen that the numerical results collapse onto this best-fitting quadratic curve represented by the above correlation, with the regression constant of $R^2 = 0.9684$. It is further observed that the effect of β is very weak (with $c = 0.038$). This is further shown by the following correlation between η and the combination of Re and α only, with the exclusion of β, in the form of $\mathrm{Re}^a\alpha^b$,

$$\eta = -115.5x^2 + 54.124x - 3.5989, \tag{20}$$

in which $x = \mathrm{Re}^{-0.104}\alpha^{-0.234}$, with $a = -0.104$ and $b = -0.234$, respectively. As shown in Fig. 28(b), it can be observed that the numerical results also collapse onto this best-fitting quadratic curve represented by this correlation, with the regression constant of $R^2 = 0.9652$ and no change or very small changes of the exponents, coefficients and constants of both correlations above.

4. Conclusion

This study numerically investigated the thermal-hydraulic behaviour of X-type lattice heat-sink structures with systematically varied strut inclination angles (strut curvature angle α over 40°–60° and inclination angle β over 30°–40°), over a wide Reynolds number range (over 2645–7936). The coupled effects of flow structure, heat transfer, pressure loss, pumping power, and overall performance efficiency were examined.

It was found that Reynolds number is the dominant flow parameter, with increasing Re leading to monotonic enhancement of the average Nusselt number due to intensified inertial effects, flow mixing, and thermal boundary-layer thinning. However, the accompanying increase in pressure drop was more pronounced, resulting in a consistent decline in the thermal-hydraulic performance factor at higher Reynolds numbers. The α angle was found to be the primary geometric parameter governing lattice performance. Decreasing α enhanced convective

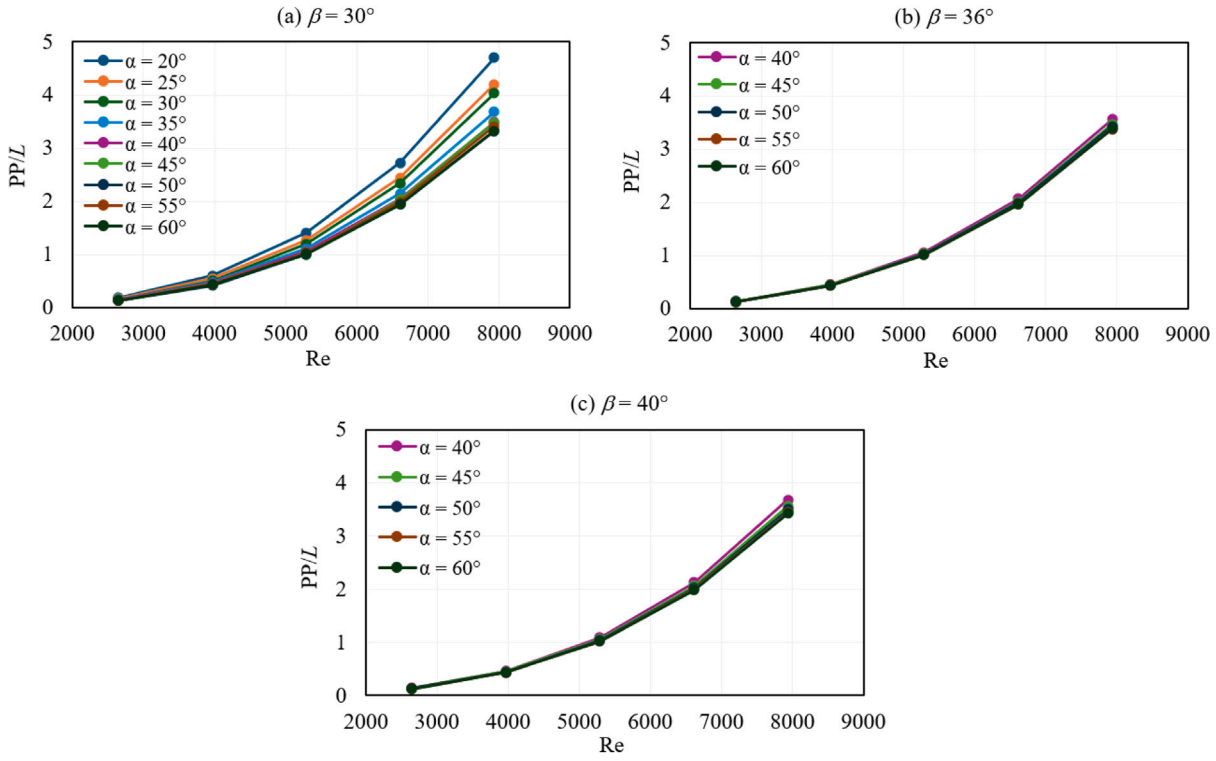


Fig. 25. PP/L plotted against Re for different lattice configurations: (a) β = 30°, (b) β = 36°, and (c) β = 40°, respectively.

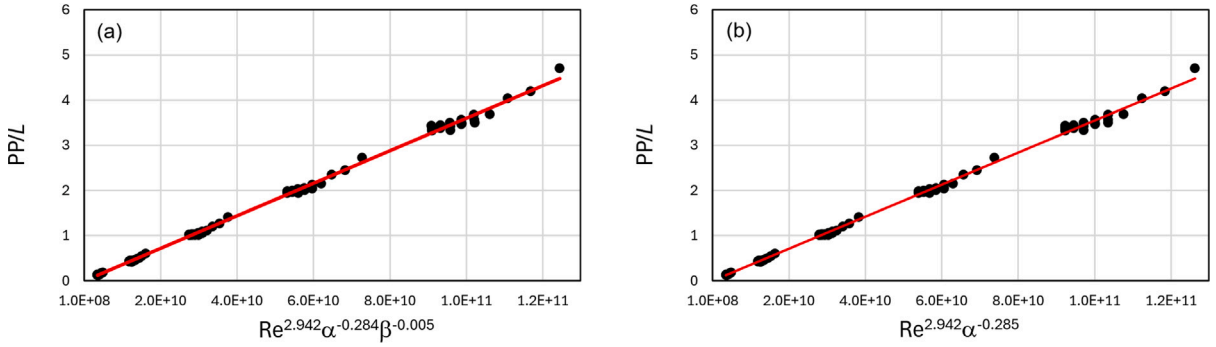


Fig. 26. (a) The correlation between PP/L and $Re^{2.942}\alpha^{-0.284}\beta^{-0.005}$ and (b) the correlation between PP/L and $Re^{2.942}\alpha^{-0.285}$, with the solid lines representing the best-fitting straight lines obtained through a multi-variable regress analysis using the obtained data from all simulation runs.

heat transfer and increased pressure drop due to stronger geometric confinement, accelerated flow through narrower inter-strut passages, and intensified fluid–solid interaction. Flow and thermal field visualizations confirmed that smaller α values promote greater velocity non-uniformity, stronger flow deflection, and steeper thermal gradients within the lattice core. From a performance perspective, small α configurations achieved better thermal-hydraulic efficiency, indicating that the heat-transfer gains outweigh the associated hydraulic penalties. In contrast, the influence of the β angle was minimal. Variations in β produced only marginal changes in the average Nusselt number, pressure drop, pumping power, and thermal-hydraulic performance. The role played by β is mainly fine-tuning the flow and thermal fields.

Overall, improved performance can be achieved at lower α values and moderate Reynolds numbers, where convective heat transfer enhancement dominates over hydraulic losses. These results demonstrate that balanced geometric design, rather than maximization of individual lattice angles or heat transfer metrics, is essential for achieving high-performance lattice heat sinks. These findings provide insight into the thermo-hydraulic behaviour of additively manufactured lattice-based thermal-management systems for compact and energy-efficient engineering applications.

Declaration of competing interest

The authors declare that they have no known competing financial interests or personal relationships that could have appeared to influence the work reported in this paper.

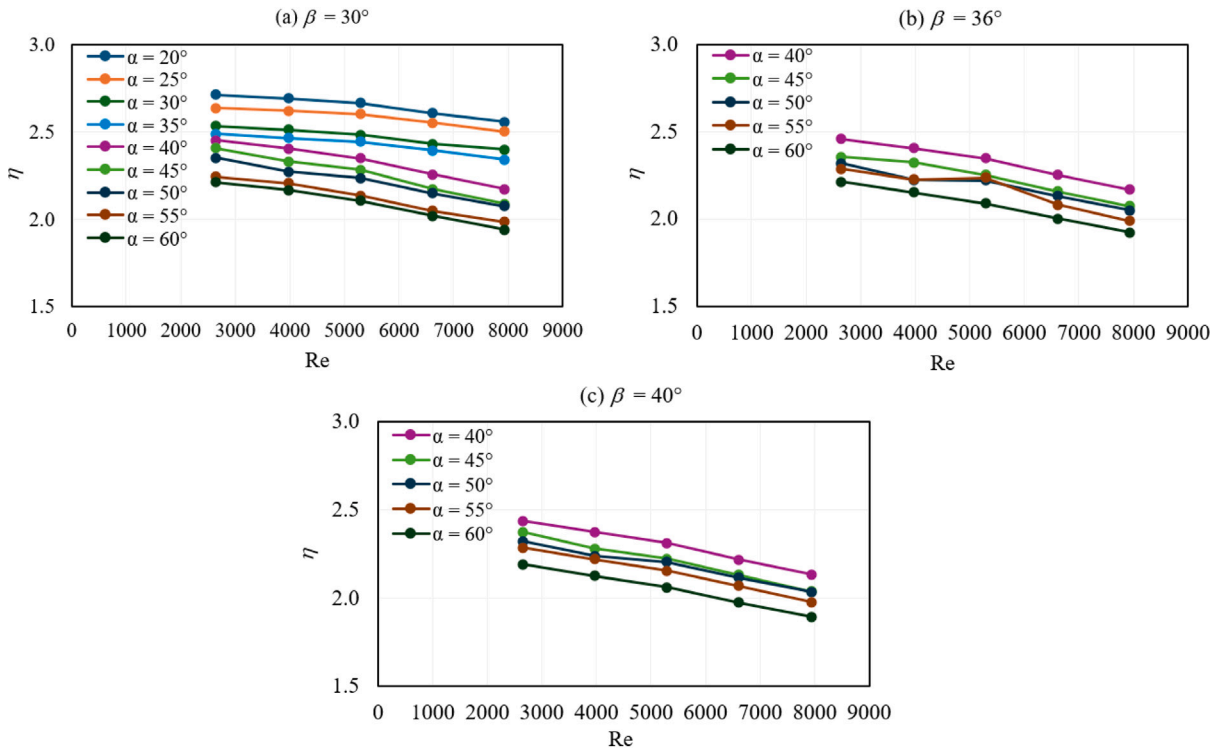


Fig. 27. η plotted against Re for different lattice configurations: (a) $\beta = 30°$, (b) $\beta = 36°$, and (c) $\beta = 40°$, respectively.

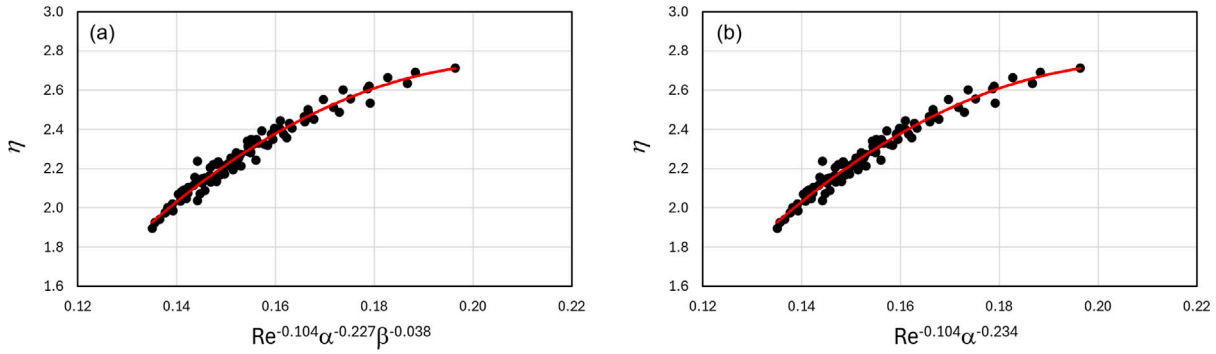


Fig. 28. (a) The correlation between η and $Re^{-0.104}\alpha^{-0.227}\beta^{-0.038}$ and (b) the correlation between η and $Re^{-0.104}\alpha^{-0.234}$, with the solid lines representing the best-fitting quadratic curves obtained through a multi-variable regress analysis using the obtained data from all simulation runs.

Data availability

Data will be made available on request.

References

[1] A. Narkhede, N. Gnanasekaran, A.K. Yadav, A novel optimized liquid cooled heat sink integrated with 3D lattice structure under different blockage ratios, Int. Commun. Heat Mass Transfer 163 (2025) 108715.
[2] M. Shahrzadi, M.D. Emami, A.H. Akbarzadeh, Heat transfer in BCC lattice materials: Conduction, convection, and radiation, Compos. Struct. 284 (2022) 115159.
[3] K.N. Son, J.A. Weibel, V. Kumaresan, S.V. Garimella, Design of multifunctional lattice-frame materials for compact heat exchangers, Int. J. Heat Mass Transfer 115 (2017) 619–629.
[4] S. Narkhede, A. Sur, R. Tiwari, The effects of topological configuration and geometric parameters on heat transfer and fluid flow characteristics of lattice-based heat sinks, Numer. Heat Transf. A: Appl. 85 (2024) 1481–1500.
[5] P. Singh, Y. Aider, M.S. Phanikumar, R.L. Mahajan, Experimental study on flow and thermal transport in additively manufactured lattices based on cube-shaped unit cell, ASME J. Heat Mass Transf. 147 (2025) 022701.
[6] P. Ekade, S. Krishnan, Fluid flow and heat transfer characteristics of octet truss lattice geometry, Int. J. Therm. Sci. 137 (2019) 253–261.
[7] A. Narkhede, N. Gnanasekaran, A.K. Yadav, Detailed thermo-hydraulic investigation of 3D octet lattice structure integrated heat sink, Int. Commun. Heat Mass Transfer 160 (2025) 108345.
[8] A. Chaudhari, P. Ekade, S. Krishnan, Experimental investigation of heat transfer and fluid flow in octet-truss lattice geometry, Int. J. Therm. Sci. 143 (2019) 64–75.
[9] Y. Ma, H. Yan, K. Hooman, G. Xie, Enhanced heat transfer in a pyramidal lattice sandwich panel by introducing pin-fins/protrusions/dimples, Int. J. Therm. Sci. 156 (2020) 106468.
[10] X. Bai, Z. Zheng, A. Nakayama, Heat transfer performance analysis on lattice core sandwich panel structures, Int. J. Heat Mass Transfer 143 (2019) 118525.
[11] X. Wang, Z. Zhong, T. Zeng, G. Xu, Y. Cui, K. Zhang, Heat transfer property of C/SiC composite pyramidal lattice core sandwich structures, Compos. Struct. 301 (2022) 116215.
[12] H. Yan, W. Wu, Z. Zhao, F. Feng, Review and comparison of turbulent convective heat transfer in state-of-the-art 3D truss periodic cellular structures, Appl. Therm. Eng. 235 (2023) 121450.
[13] T. Dixit, P. Nithiarasu, S. Kumar, Numerical evaluation of additively manufactured lattice architectures for heat sink applications, Int. J. Therm. Sci. 159 (2021) 106607.
[14] Y. Aider, I. Kaur, H. Cho, P. Singh, Periodic heat transfer characteristics of additively manufactured lattices, Int. J. Heat Mass Transfer 189 (2022) 122692.

[15] C. Guo, J. Zhao, M. Liao, F. Tan, Y. Li, Z. He, Heat transfer performance of different lattice structures in porous medium combustion, Case Stud. Therm. Eng. 72 (2025) 106250.
[16] J.Y. Ho, K.C. Leong, T.N. Wong, Experimental and numerical investigation of forced convection heat transfer in porous lattice structures produced by selective laser melting, Int. J. Therm. Sci. 137 (2019) 276–287.
[17] X. Jin, B. Shen, H. Yan, B. Sunden, G. Xie, Comparative evaluations of thermofluidic characteristics of sandwich panels with X-lattice and pyramidal-lattice cores, Int. J. Heat Mass Transfer 127 (2018) 268–282.
[18] H.B. Yan, Q.C. Zhang, T.J. Lu, T. Kim, A lightweight X-type metallic lattice in single-phase forced convection, Int. J. Heat Mass Transfer 83 (2015) 273–283.
[19] M. Abdelhamid, A. Czekanski, Impact of the lattice angle on the effective properties of the octet-truss lattice structure, J. Eng. Mater. Technol. 140 (2018) 041010.
[20] M.A. El-Sayed, K. Essa, M. Ghazy, H. Hassanin, Design optimization of additively manufactured titanium lattice structures for biomedical implants, Int. J. Adv. Manuf. Technol. 110 (2020) 2257–2268.
[21] A.W. Date, Introduction to Computational Fluid Dynamics, Cambridge University Press, 2005.
[22] J. Ernot, P.G. Verdin, H. Ahmad, P. Indge, Analytical and numerical predictions of the thermal performance of multi-layered lattice structures, Int. J. Heat Mass Transfer 145 (2019) 118752.
[23] H. Liu, Q.N. Yu, Z.G. Qu, R.Z. Yang, Simulation and analytical validation of forced convection inside open-cell metal foams, Int. J. Therm. Sci. 111 (2017) 234–245.
[24] H. Yan, X. Yang, T. Lu, G. Xie, Convective heat transfer in a lightweight multifunctional sandwich panel with X-type metallic lattice core, Appl. Therm. Eng. 127 (2017) 1293–1304.
[25] Q. Fu, X. Luo, W. Chen, M.K. Chyu, Numerical investigation of the effects of lattice array structures on film cooling performance, Energies 15 (13) (2022) 4711.
[26] R.L. Webb, E.R.G. Eckert, Application of rough surfaces to heat exchanger design, Int. J. Heat Mass Transfer 15 (9) (1972) 1647–1658.
[27] H. Wang, C. Zhao, W. Liu, Z. Liu, H. Bian, K. Zhang, Advances in triply periodic minimal surface structures for thermal management systems: A comprehensive review, Appl. Therm. Eng. 279 (2025) 127481.
[28] D. Nagy, Á. Gyenge, B. Farkas, D. Réfy, Validation of a new propellant valve test bed to support developments for shattered pellet injection technology, Fusion Eng. Des. 218 (2025) 115142.
[29] M. Öztürk, E. Çiftçi, Numerical analysis of a helically coiled tube heat exchanger performance utilized in molten salt nuclear reactors for molten salt and He-CO_2 working fluid conditions, Prog. Nucl. Energy 187 (2025) 105844.
[30] A. Jones, J. Darabi, Effect of fin geometry on the thermal performance of a phase change material heatsink, Appl. Therm. Eng. 236 (2024) 121973.
[31] Y. Aider, P. Singh, Experimental study on flow and thermal transport in additively manufactured architectured lattice frame with air and particles as convective agents, J. Therm. Sci. Eng. Appl. 17 (5) (2025) 051006.
[32] K. Park, B.-s. Kang, S. Kim, Influence of design parameters on natural convection heat transfer in additively manufactured body centered cubic lattice structures, Int. J. Therm. Sci. 205 (2024) 109250.
[33] E. Vaglio, F. Scalzo, N. Scussolin, L. Casarsa, Experimental investigation of heat transfer and pressure losses across additively manufactured body centered cubic arrays: Effects of cell shape and array arrangement, Appl. Therm. Eng. 280 (2025) 128253.
[34] H. Yan, K. Fang, W.-T. Wu, Z. Zhao, F. Feng, Thermal performance enhancement by modifying the spiral flow and turbulence transport in an X-lattice cellular structure, Int. J. Therm. Sci. 205 (2024) 109277.
[35] I. Kaur, P. Singh, Effects of inherent surface roughness of additively manufactured lattice frame material on flow and thermal transport, Int. J. Heat Mass Transfer 209 (2023) 124077.
[36] L. Bernardini, S. Piacquadio, K.-U. Schröder, M. Mameli, P. Di Marco, S. Filippeschi, Exploring the impact of unit cell size on fluid dynamics in lattice structures: Experimental and numerical insights, Int. J. Thermofluids (2025) 101543.
[37] M. Aghaei-Jouybari, J.-H. Seo, S. Pinto, L. Cattafesta, C. Meneveau, R. Mittal, Extended Darcy–Forchheimer law including inertial flow deflection effects, J. Fluid Mech. 980 (2024) A13.
[38] M. Ho, L.-L. Tan, Y. Hung, C. Oon, Thermohydraulic and irreversibility analyses of swirl flows utilizing distorted radial fins: Entropy generation and entransy dissipation evaluation, Int. J. Energy Res. 2023 (1) (2023) 5557828.